

Elevating cytosolic NADPH metabolism in endothelial cells ameliorates vascular aging

Received: 5 December 2024

Dan Wu^{1,2,7}, Bo Tan^{①,3,7}, Zijie Cheng¹, Haoqi Li¹, Huimin Li², Yun Yin², Fenfen Ma⁴, Tao Chen⁵, Xin Dong^{①,6}, Wang Wang⁶ & Qingxun Hu^{①,✉}

Accepted: 23 September 2025

Published online: 03 November 2025

 Check for updates

Reduced nicotinamide adenine dinucleotide phosphate (NADPH) metabolism is independently regulated in different compartments in endothelial cells (EC). The metabolic profile and functional impact of NADPH during EC senescence remain largely unknown. Using a genetically encoded fluorescent indicator, we find that cytosolic, but not mitochondrial, NADPH level increases during EC senescence. Upregulation of glucose-6-phosphate dehydrogenase (G6PD) further elevates cytosolic NADPH level during EC senescence. Suppression of G6PD S-nitrosylation at C385 potentiates G6PD activity. G6PD overexpression alleviates, while its knockdown aggravates, vascular aging. NADPH is indispensable for G6PD to protect against vascular aging through increasing reduced glutathione and inhibiting HDAC3 activity. Among 1419 FDA-approved drugs, folic acid, catalyzed by methylenetetrahydrofolate dehydrogenase to generate NADPH, effectively alleviates vascular aging in angiotensin II-infused mice and naturally aged mice. The connection between NADPH metabolism and EC senescence provides a unique angle for understanding vascular aging and an efficient target for therapy.

Cardiovascular disease is a leading cause of death globally and its mortality rate increases with age¹. Since the number of adult aged 65 and above is expected to double in the next 30 years, age-related vascular diseases become an important determinant to human healthspan. Age-related cardiovascular diseases are featured by changes in arterial function or phenotype. Moreover, microcirculation possesses a unique ability to influence the microenvironment of majority of the organs. Thus, understanding the molecular mechanisms of vascular aging is central to tackle age-related cardiovascular disease². Vascular endothelium is a single layer of cells covering the lumen of vascular vessels and plays an important role in maintaining vascular homeostasis. Numerous studies suggest that senescence of vascular endothelial cells (ECs) leads to initiation and progression of cardiovascular diseases^{3–5}. Because central carbon metabolism is

necessary for EC function and metabolic reprogramming is a hallmark for EC senescence^{6,7}, a better understanding of how metabolism impacts EC senescence is urgently needed for developing treatments for vascular aging.

Nicotinamide adenine dinucleotide phosphate (NADP, oxidized form: NADP⁺, reduced form: NADPH) has long been recognized as a key cofactor for redox defense and reductive biosynthesis⁸. Increasing evidence shows that the balance between reactive oxygen species (ROS) and NADPH-mediated redox is a critical factor in EC senescence. In senescent EC, the activity of NADPH oxidase was significantly increased, causing elevated ROS production through oxidizing NADPH. ROS further reacted with nitric oxide (NO) to generate ONOO[–]^{5,9}. Inhibiting the activity of NADPH oxidase significantly abrogated EC senescence¹⁰. Moreover, NADPH promotes glutathione

¹Shanghai Engineering Research Center of Organ Repair, School of Medicine, Shanghai University, Shanghai, China. ²Department of Pharmacy, Tongji Hospital, Tongji University School of Medicine, Shanghai, China. ³Laboratory of Clinical Pharmacokinetics, Institute of Clinical Pharmacology, Shuguang Hospital Affiliated to Shanghai University of Traditional Chinese Medicine, Shanghai, China. ⁴Department of Pharmaceutics, School of Pharmacy, Shanghai Pudong Hospital, Fudan University, Shanghai, China. ⁵Qinghai Key Laboratory of Qinghai-Tibet Plateau Biological Resources, Chinese Academy of Science, Northwest Institute of Plateau Biology, Xining, China. ⁶Mitochondria and Metabolism Center, Department of Anesthesiology and Pain Medicine, University of Washington, Seattle, WA, US. ⁷These authors contributed equally: Dan Wu, Bo Tan. ✉e-mail: qingxh@shu.edu.cn

and thioredoxin oxidation-reduction systems to effectively attenuate excessive ROS production during EC senescence¹¹. Given the important role of NADPH in redox system, research has been focused on the regulatory function of NADPH oxidoreductase. The metabolic profiles of NADPH in EC senescence and the potential regulatory role of NADPH-related metabolic pathways in vascular aging remain largely unexplored.

Intracellular NADPH consumption and production in different compartments are independently regulated¹². In EC, NADPH can be generated by three pathways: glucose-6-phosphate dehydrogenase (G6PD) and 6-phosphogluconate dehydrogenase (PGD) in oxidative pentose phosphate pathway (oxPPP), malic enzymes (MEs) in glutaminolysis, and methylenetetrahydrofolate dehydrogenase (MTHFD) in folate metabolism. oxPPP is the major pathway for NADPH generation in ECs and it critically regulates EC function^{11,13}. For example, oxPPP in ECs promoted vascular maturation by controlling vascular matrix composition¹⁴. oxPPP was significantly enhanced in highly proliferative ECs to meet the demand for cell proliferation^{7,15}. Blockade of oxPPP reprogramed EC metabolism towards glycolysis and worsened inflammatory responses in pulmonary artery ECs¹⁶.

G6PD, a rate-limiting enzyme in oxPPP, plays a critical role in regulating cell senescence in age-related animal models. For example, the activity of G6PD was significantly decreased in high-glucose-induced EC senescence, leading to decreased endothelial nitric oxide synthase (eNOS) activity and reduced antioxidant capacity¹⁷. G6PD activity decreased in oxidants-induced fibroblast senescence and ablation of G6PD further aggravated fibroblast senescence¹⁸. Overexpression of G6PD protein significantly alleviated age-related mouse hearing loss¹⁹ and prolonged the lifespan of female mice²⁰. Although the beneficial role of G6PD in aging has been established, the downstream mechanism that mediates G6PD's effects in antagonizing EC senescence remain unknown.

While traditional enzymatic cycling assays, mass spectrometry and chromatography have been used to monitor whole-cell NADPH pool, they require cell homogenization and cannot differentiate compartmental NADPH pools, where it regulates distinct functions²¹. Here, we employed a highly responsive and genetically encoded NADPH sensor (iNap1)²² and revealed that cytosolic NADPH was elevated during EC senescence. Decreased NO concentration promoted G6PD de-S-nitrosylation at C385 and increased its activity, leading to elevated NADPH levels. G6PD overexpression significantly elevated NADPH level, inhibited glutathione oxidation and histone deacetylase 3 (HDAC3) activity, and suppressed EC senescence and vascular aging. These results suggest that G6PD/NADPH pathway is upregulated by stimulators of vascular aging, and it plays a causal role in limiting endothelial cell aging. Furthermore, iNap1 allowed high-throughput metabolic screening of 1419 drugs approved by the Food and Drug Administration, among which folic acid (FA) significantly elevated NADPH content via MTHFD1 and augmented vascular activity in naturally aged mice. These findings highlight a beneficial role of endothelial NADPH metabolism in vascular aging.

Results

Real-time monitoring of cytosolic and mitochondrial NADPH in primary cultured human aortic endothelial cells

To determine compartmentalized NADPH levels, we overexpressed an NADPH indicator, iNap1 in either cytosol (cyto-iNap1) or mitochondria (mito-iNap3) of primary cultured human aortic endothelial cells (HAECS). We also constructed the nonresponsive variant, iNapc to normalize iNap fluorescence. Fluorescence of these indicators were collected upon 405 nm (or 420 nm) and 488 nm (or 485 nm) excitation, and their ratio (405/488 or 420/485) was used to reflect NADPH level²². Confocal imaging in primary cultured HAECS revealed clear patterns of cytosolic or mitochondrial localization of the indicators (Fig. 1a, b). For in situ calibration, 0.001% or 0.3% digitonin was used to

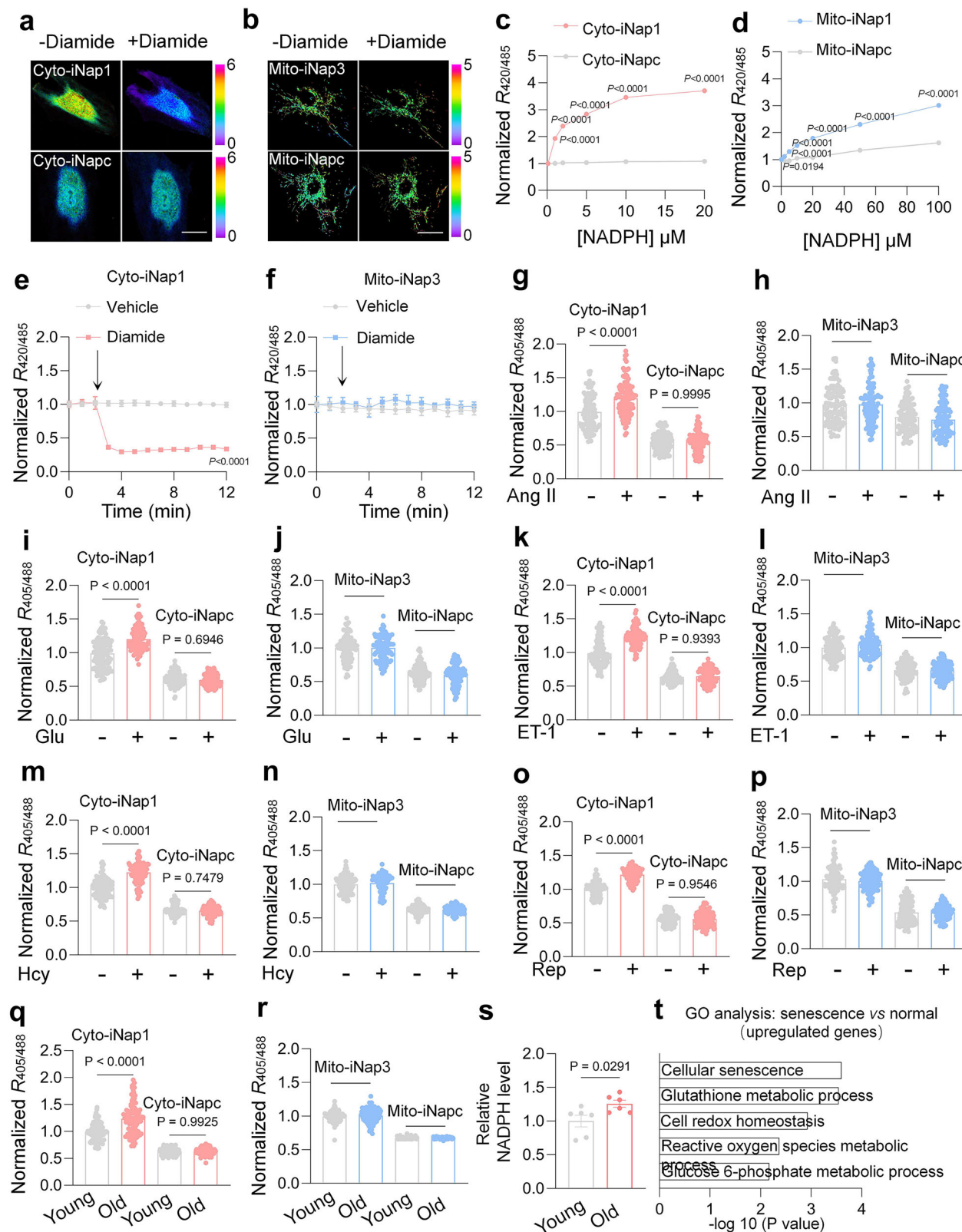
permeabilize the plasma membrane or mitochondrial inner membrane of HAECS, respectively. Then, the cells were exposed to increasing concentrations of NADPH. iNap1 responded linearly to a wide range of NADPH concentrations, while iNapc was nonresponsive (Fig. 1c-d). Diamide (100 μ M), a strong oxidant, lowered cyto-iNap1, but not mito-iNap3, fluorescence (420/485 ratio), indicating a stronger antioxidant capacity of mitochondrial NADPH redox system (Fig. 1a, b, e, f). Diamide induced no change in iNapc fluorescence in both compartments (Supplementary Fig. 1a-b). These observations verified that iNap is a specific NADPH indicator and can monitor subcellular NADPH concentrations in live HAECS.

Nicotinamide adenine dinucleotide (NAD, oxidized form: NAD⁺, reduced form: NADH) has been shown to play an important role in vascular aging²³. To explore whether compartmental NAD(H) is changed during EC senescence, we first tested the use of an NADH/NAD⁺ ratio indicator (SoNar) for analyzing cytosolic and mitochondrial NADH/NAD⁺ ratios, using cpYFP as control²⁴. Like iNap, cyto-SoNar and mito-SoNar located in cytosol or mitochondria of HAECS, respectively (Supplementary Fig. 1c, d). In situ titration in permeabilized HAECS showed that cyto-SoNar and mito-SoNar responded linearly to changes in NADH/NAD⁺ ratios and cpYFP is not responsive (Supplementary Fig. 1e, f). Diamide decreased, while rotenone increased, both cyto-SoNar and mito-SoNar fluorescence (420/485 ratio, Supplementary Fig. 1c, d, g, j). Moreover, cyto-SoNar responded to sequential treatments of pyruvate (1 mM) and oxamate (5 mM), while mito-SoNar exhibited opposite responses to β -hydroxybutyrate (β -OHB, 1 mM) and acetoacetic acid (AcAc, 1 mM) (Supplementary Fig. 1k, l). These data demonstrate that SoNar can monitor subcellular NADH/NAD⁺ ratios.

Elevated cytosolic, but not mitochondrial, NADPH concentration during EC senescence

Angiotensin II (Ang II) signaling is closely associated with age-related changes in arterial structure and function. Increased Ang II level accelerates arterial aging and the development of age-related phenotypes²⁵. Therefore, we adopted the use of Ang II as a stimulator of EC senescence in HAECS²⁶. First, we monitored the dose- and time-dependent effects of Ang II on mRNA level of p16 (an aging biomarker) and determined the optimal condition (2 μ M for 72 hr) for Ang II-induced senescence in HAECS (Supplementary Fig. 2a, b). Under this condition, we found that β -galactosidase staining (Supplementary Fig. 2c), protein levels of p16, p21 and VCAM-1 (Supplementary Fig. 2d), and mRNA levels of senescence-associated secretory phenotype (SASP) factors (IL-1 β , IL-6, IL-8 and CXCL1, Supplementary Fig. 2e) were all significantly increased. These results confirmed that Ang II effectively induced senescent phenotypes in primary cultured HAECS.

To evaluate the metabolic profile of NADPH in EC senescence, we used iNap and different vascular aging models. First, Ang II (2 μ M for 72 h) increased cytosolic, but not mitochondrial, NADPH levels in primary cultured HAECS (Fig. 1g, h). Similar results were obtained from high glucose (Glu, 25 mM, 48 h), endothelin-1 (ET-1, 10 nM, 48 h), or homocysteine (Hcy, 50 μ M, 72 hr)-induced HAECS senescence models and replicative EC senescence models (Fig. 1i-p and Supplementary Fig. 2f). Importantly, cytosolic NADPH level was increased in isolated ECs from thoracic aorta of old (18 months) mice as compared to young (4 months) mice (Fig. 1q, r). Consistently, NADPH content was higher in thoracic aorta of naturally aged mice (24 months old) compared to young mice (4 months old) (Fig. 1s). We also found that plasma NADPH levels trended up in humans as they get older (Supplementary Fig. 2g), in line with a previous report²⁷. Furthermore, NADP⁺ content trended low in Ang II-induced senescent ECs and naturally aged ECs (Supplementary Fig. 2h, i). Finally, we conducted microarray analysis of senescent HAECS. Gene ontology (GO) analysis indicated that pathways related to redox regulation were significantly upregulated in



senescent HAECS (Fig. 1t). Taken together, these results support that NADPH levels are elevated in the senescent EC.

It has been shown that NAD⁺ level decreased during aging²³. We found that NAD⁺ level was much lower in thoracic aorta of naturally aged mice as compared to young mice (Supplementary Fig. 2j), and NAD⁺ content in human plasma trended downward with increased age (Supplementary Fig. 2k). However, NADH/NAD⁺ ratio declined in

cytosol but increased in mitochondria during HAECS senescence (Supplementary Fig. 2l, m), which may underlie the opposite changes of NADH/NAD⁺ ratio in cytosol and mitochondria. Moreover, we also used an NADH indicator (Frex)²⁸ to analyze cytosolic and mitochondrial NADH levels. Ang II decreased cytosolic and mitochondrial NADH levels in primary cultured HAECS (Supplementary Fig. 2n, o). GO and Kyoto encyclopedia of genes and genomes (KEGG) analysis revealed

Fig. 1 | iNap1 detected increased cytosolic but not mitochondrial NADPH levels in senescent ECs. Representative images of the fluorescence ratio of cyto-iNap1 and cyto-iNapc (a), mito-iNap3 and mito-iNapc (b) in HAECS upon diamide treatment. Scale bar: 10 μ m. Response of the fluorescence ratio of cyto-iNap1 and cyto-iNapc (c), mito-iNap3 and mito-iNapc (d) to various NADPH concentrations in permeabilized HAECS. $n = 3$ biologically independent samples. Time-dependent changes in cyto-iNap1 (e) and mito-iNap3 (f) in response to acute addition of diamide. $n = 3$ biologically independent samples. The fluorescence ratio of cyto-iNap1 and cyto-iNapc, mito-iNap3 and mito-iNapc with or without Ang II (g, h), Glu (i, j), ET-1 (k, l), Hcy (m–n) and replicative passage (o, p) treatment. $n = 3$ biologically independent samples, 106, 112, 101 and 101 cells (g), 110, 99, 107 and 105 cells (h),

122, 112, 118 and 126 cells (i), 109, 115, 117 and 117 cells (j), 104, 104, 107 and 105 cells (k), 102, 104, 114 and 116 cells (l), 105, 108, 105 and 106 cells (m), 106, 105, 106 and 104 cells (n), 122, 122, 122 and 105 cells (o), 112, 118, 120 and 103 cells (p). The fluorescence ratio of cyto-iNap1 and cyto-iNapc (q), mito-iNap3 and mito-iNapc (r) in young and old ECs. $n = 3$ biologically independent samples, 125, 108, 110, and 118 cells (q) and 104, 115, 122 and 122 cells (r). s Relative NADPH content in thoracic aorta from young and old mice. $n = 6$ mice. t GO analyses of microarray data of old vs young HAECS. Data are presented as mean values \pm SEM. Statistical significance was assessed by Two-way ANOVA followed by Šídák's multiple comparisons test (c–f), One-way ANOVA followed by Tukey's multiple comparisons test (g–r), two-tailed unpaired Student *t* test (s).

downregulation of glucose and glycolysis metabolism in senescent HAECS (Supplementary Fig. 2p, q). Acute incubation of glucose (20 mM) did not change NADPH levels in cytosol or mitochondria of HAECS (Supplementary Fig. 2r, s). However, glucose acutely increased both cytosolic and mitochondrial NADH/NAD⁺ ratio in normal but not senescent HAECS (Supplementary Fig. 2t, u). Therefore, compartmentalized NAD(H) metabolism and NADPH metabolism are distinctly regulated in ECs.

G6PD de-S-nitrosylation elevated NADPH level during EC senescence

NAD(H) metabolism has been widely studied in aging, but the role of NADPH metabolism in EC senescence remains elusive. To explore why cytosolic NADPH level increased during EC senescence, we examined the protein levels of NADPH-generating enzymes in primary cultured HAECS, including G6PD and PGD in pentose phosphate pathway, IDH1 in citric acid cycle, ME1 in malate-aspartate shuttle, MTHFD1 in folate metabolism, and NAD kinase (NADK) (Supplementary Fig. 3a). Intriguingly, only G6PD was increased in a dose- and time-dependent manner by Ang II incubation (Fig. 2a, b and Supplementary Fig. 3b, c). Moreover, the activity of G6PD was significantly increased during HAECS senescence and DHEA suppressed this increase (Supplementary Fig. 3d). G6PD protein level was also much higher in ECs isolated from thoracic aorta of naturally aged mice (24 months old) compared to young mice (4 months old) (Fig. 2c and Supplementary Fig. 3e). Moreover, G6PD protein level was increased in high glucose-induced senescence or replicative EC senescence models (Supplementary Fig. 3f, g). These results indicate that the increased cytosolic NADPH level may be due to elevated G6PD protein level and activity during EC senescence.

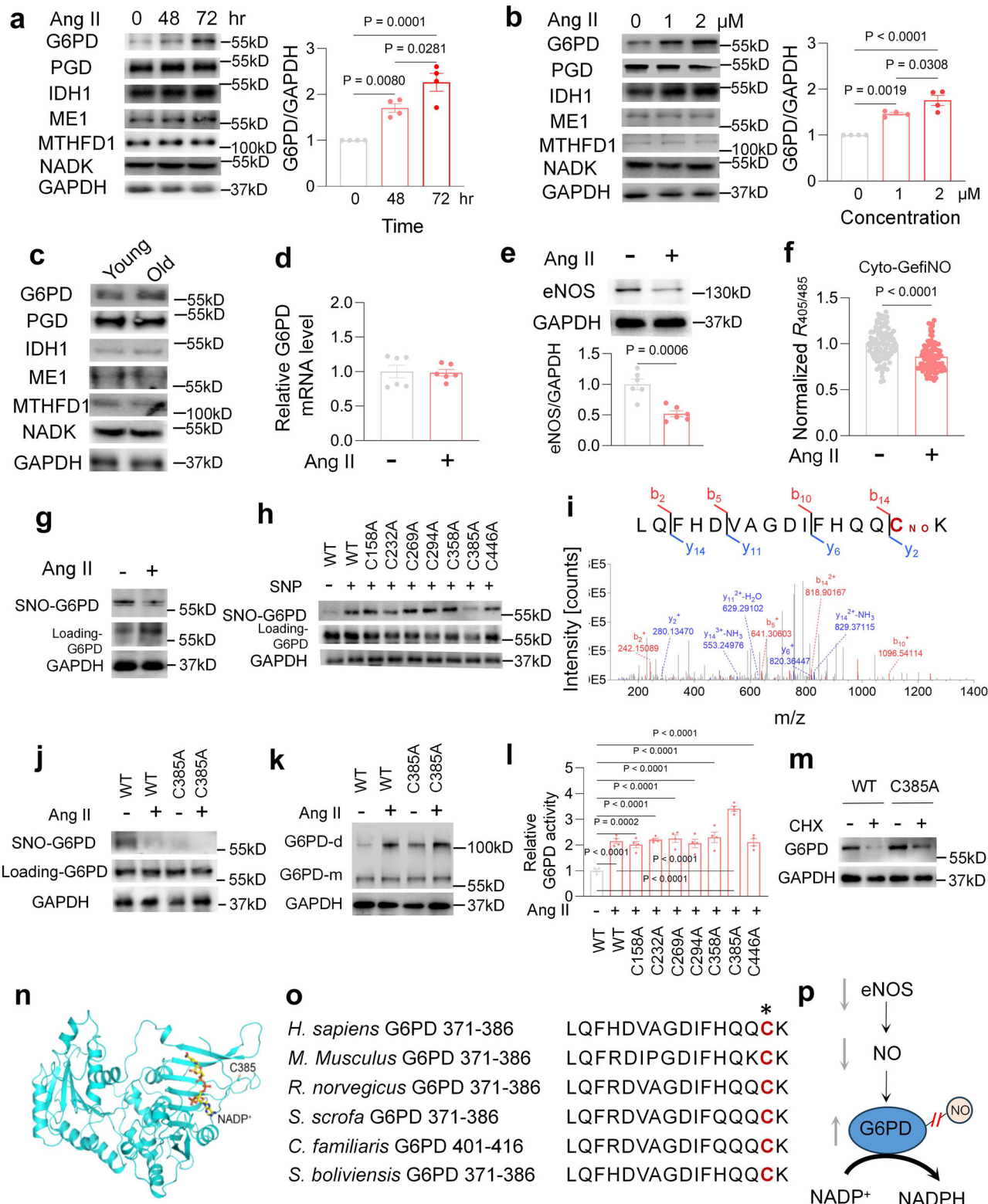
Next, we determined why G6PD protein level was increased during EC senescence. Ang II did not impact the mRNA level of G6PD, suggesting that transcription regulation is unlikely a mechanism (Fig. 2d). Therefore, we hypothesized that post-translational modification and degradation suppression may be responsible for the increased G6PD protein level. To test this hypothesis, we first determined NO concentration because NO is highly enriched in ECs, can modulate protein activity/stability through S-nitrosylation, and its level decreases during EC senescence^{5,29}. Indeed, Ang II significantly decreased cytosolic NO levels measured by a biosensor, cyto-GefiNO³⁰, the contents of nitrite, which is a stable breakdown product of NO, and eNOS protein levels (Fig. 2e, f and Supplementary Fig. 3h). Moreover, Ang II also suppressed S-nitrosylation of total proteins and G6PD in senescent HAECS (Fig. 2g and Supplementary Fig. 3i, j). To exclude nonspecific background signals, we performed the biotin-switch experiment in the absence of ascorbate, which led to nearly complete loss of the signal, verifying that it is specific for G6PD S-nitrosylation (Supplementary Fig. 3k). To identify the specific cysteine residues on G6PD that was de-S-nitrosylated, we generated 7 single point mutations (C to A) of human G6PD protein to mimic non-S-nitrosylated status without altering amino acid structure. After transfection into HEK293 cells, WT and mutations of G6PD had similar expression level (Supplementary Fig. 3l). Biotin-switch assay revealed

that sodium nitroprusside (SNP, a NO donor) elevated S-nitrosylation levels in WT and most of the mutations of G6PD, except the C385A mutation, suggesting that C385 is the residue modified by NO (Fig. 2h and Supplementary Fig. 3m). To demonstrate whether this site is S-nitrosylated in live cells, we performed liquid chromatography-mass spectrometry (LC-MS) study using whole cell homogenates after enriching G6PD. S-nitrosylated or biotin-HPDP labeled C385 residue was found in normal cultured HAECS but not in Ang II-incubated senescent HAECS (Fig. 2i and Supplementary Fig. 3n). These data provide strong evidence that G6PD is de-S-nitrosylated at C385 during HAECS senescence.

To investigate how de-S-nitrosylation affected G6PD activity, we overexpressed WT and C385A mutation of G6PD in HAECS for 48 hr. As expected, S-nitrosylation level of G6PD C385A mutation was lower than that of WT G6PD (Fig. 2j and Supplementary Fig. 3o). G6PD dimer formation was increased in G6PD C385A mutation transduced cells as compared to WT G6PD transduced cells (Fig. 2k and Supplementary Fig. 3p). In line with these results, the activity of G6PD C385A was higher than that of WT G6PD in untreated ECs (Supplementary Fig. 3q), and the difference was bigger after Ang II treatment (Fig. 2l). These results suggest that de-S-nitrosylation at C385 promoted G6PD activity. Next, we investigated whether de-S-nitrosylation at C385 is responsible for the increased G6PD protein level induced by Ang II. Cycloheximide (CHX) is a translation inhibitor that blocks protein synthesis. CHX incubation significantly decreased the protein levels of WT but not C385A mutation of G6PD (Fig. 2m and Supplementary Fig. 3r), indicating that de-S-nitrosylation at C385 suppresses G6PD degradation. In the 3D protein structure of G6PD, C385 locates on the surface and in a flexible loop of C terminal within the G6PD dimerization interface (Fig. 2n). The large residue (nitrosylated C385) is sterically hindered, while de-nitrosylated C385 is smaller and may interact with D379 and Q383 to form a hydrogen bond network and stabilize the G6PD protein structure (Supplementary Fig. 3s). These interaction may potentiate G6PD dimerization, activity, and stability (Fig. 2k–m). Moreover, it has been shown that I392, R393, V394 and K403 are in the β sheet critical for binding NADP^{31–33}. C385 is located immediately before the β sheet and within the dimerization interface. Thus, nitrosylation and de-S-nitrosylation of C385 can impact the mainchain conformation, the dimer interface, and the activity of G6PD. C385 is highly conserved across different species, indicating that this residue is critical for regulating G6PD function (Fig. 2o). Taken together, the above results suggest that decreased NO concentration promotes G6PD de-S-nitrosylation at C385 to increase its protein stability and activity (Fig. 2p).

Upregulation but not downregulation of G6PD alleviated EC senescence

Since NADPH generation via G6PD was increased during EC senescence, we investigated whether downregulation of G6PD can impact cell senescence. We constructed a specific small hairpin RNA (shRNA) targeting human G6PD (shG6PD), which significantly decreased cytosolic iNap1 fluorescence by ~50% (Fig. 3a) and lowered G6PD protein levels and activity in HAECS (Fig. 3b, c and Supplementary Fig. 4a).



Moreover, shG6PD prevented the increases in NADPH level, G6PD protein level, G6PD oligomerization and G6PD activity induced by Ang II (Fig. 3a-c and Supplementary Fig. 4b). Interestingly, shG6PD exacerbated, rather than ameliorated, Ang II-induced HAEC senescence as reflected by increased β -galactosidase, reduced cell proliferation (Fig. 3d, e and Supplementary Fig. 4c, d), elevated protein levels of senescence biomarkers (p16, p21 and VCAM-1), and increased mRNA levels of core SASP genes (IL-1 β , IL-6, CCL2, ICAM and MMP9) (Fig. 3b, f and Supplementary Fig. 4a). These results suggest that Ang II-induced

G6PD upregulation is unlikely detrimental but may be beneficial to HAECS senescence.

Next, we constructed lentivirus containing G6PD (Lv-G6PD) to determine whether upregulation of G6PD can prevent EC senescence. Lv-G6PD markedly increased iNap1 fluorescence and G6PD protein levels in HAECS (Fig. 3g and Supplementary Fig. 4e). Ang II incubation further elevated iNap1 fluorescence and G6PD protein level in G6PD-overexpressing HAECS. G6PD overexpression suppressed Ang II-induced EC senescence as shown by decreased

Fig. 2 | G6PD de-S-nitrosylation at C385 increased its activity on EC senescence. The time- (a) and dose-dependent (b) effects of Ang II on G6PD, PGD, IDH1, ME1, MTHFD1 and NADK protein levels in HAECS. *n* = 4 biologically independent samples. c G6PD, PGD, IDH1, ME1, MTHFD1 and NADK protein levels in ECs isolated from thoracic aorta of young or old mice. d G6PD mRNA levels in HAECS with or without Ang II incubation. *n* = 6 biologically independent samples. e eNOS protein levels in HAECS with or without Ang II incubation. *n* = 6 biologically independent samples. f The fluorescence ratio of cyto-GefiNO with or without Ang II incubation. *n* = 3 biologically independent samples, 101 and 100 cells for respective groups. g G6PD S-nitrosylation levels in HAECS with or without Ang II incubation. h The effect of SNP on the S-nitrosylation levels of overexpressed wild type (WT) or mutations of G6PD in HEK293 cells. i Mass spectrometry analysis of G6PD S-nitrosylation showing the tandem mass spectrum of a G6PD fragment containing

the S-nitrosylated C385 (increased by 29 Da) in HAECS. The effect of Ang II on S-nitrosylation (j) and oligomerization (k) of overexpressed WT or C385A of G6PD in HAECS. l Relative activity of overexpressed WT or C385A of G6PD in HAECS with or without Ang II incubation. *n* = 4 biologically independent samples. m The degradation of G6PD WT or C385A in HAECS with or without Ang II and cycloheximide incubation. n Homology modeling of human G6PD (PDB: 6EO8) with NADP⁺ showing C385 location at α helix. o Comparison of G6PD sequences among different G6PD homologous. p Schematic model showing decreased eNOS protein and NO levels de-S-nitrosylated G6PD and augmented its activity. Data are presented as mean values \pm SEM. Statistical significance was assessed by One-way ANOVA followed by Tukey's multiple comparisons test (a, b, l), two-tailed unpaired Student *t* test (d–f).

β -galactosidase and increased cell proliferation (Fig. 3h, i and Supplementary Fig. 4f, g). Moreover, overexpression of G6PD in ECs isolated from thoracic aorta of old mice (18 months) also suppressed β -galactosidase (Fig. 3j and Supplementary Fig. 4h) and senescent biomarkers contents (p16, p21 and VCAM-1) (Fig. 3k and Supplementary Fig. 4i). We also overexpressed G6PD C385A mutant (Lv-C385) in Ang II treated HAECS. Consistent with the effect of Lv-G6PD, Lv-C385 significantly increased iNap1 fluorescence and G6PD protein levels, decreased protein levels of senescence biomarkers (p16, p21 and VCAM-1), mRNA levels of core SASP genes (IL-1 β , IL-6, CCL2, ICAM and MMP9) and β -galactosidase activity, and potentiated EC proliferation (Supplementary Fig. 4j–n). These results demonstrate that upregulation of G6PD-mediated NADPH generation effectively alleviates EC senescence.

Cytosolic, but not mitochondrial, NADPH alleviated EC senescence

G6PD is not only responsible for NADPH production but also plays an important role in signaling transduction through binding with other proteins^{34–36}. To further validate whether the anti-aging effect of G6PD is attributed to NADPH metabolism, we employed a genetically encoded tool named triphosphopyridine nucleotide oxidase (TpNOX) to directly oxidize NADPH to NADP⁺³⁷. First, we constructed lentivirus containing cytosolic located TpNOX (Lv-TpNOX) and infected primary cultured HAECS for 2 days. Lv-TpNOX depleted cytosolic NADPH content in normal cultured HAECS and prevented NADPH elevation in Ang II-treated HAECS with or without Lv-G6PD (Fig. 4a). Lv-TpNOX did not change G6PD protein level (Fig. 4b and Supplementary Fig. 5a), suggesting that TpNOX effectively consumed NADPH bypassing G6PD. Subsequently, the protein levels of senescence biomarkers (p16, p21 and VCAM-1) and mRNA levels of SASP genes (IL-1 β , IL-6, IL-8 and CXCL1) were more significantly elevated in HAECS overexpressing TpNOX with or without Lv-G6PD (Fig. 4b, c and Supplementary Fig. 5b, c). Consistently, ablation of NADPH by TpNOX overexpression modestly increased β -galactosidase activity (Fig. 4d and Supplementary Fig. 5d) and significantly suppressed proliferation of Ang II-induced HAECS (Fig. 4e and Supplementary Fig. 5e). Moreover, TpNOX overexpression abrogated the protective effects of G6PD overexpression on EC senescence (Fig. 4d–e and Supplementary Fig. 5d–e). These results indicate that the anti-aging effects of G6PD are mediated by cytosolic NADPH in HAECS.

To determine whether mitochondrial NADPH plays a role in EC senescence, we constructed lentivirus containing mitochondrial located isocitrate dehydrogenase 2 (IDH2), a key enzyme for NADPH generation in mitochondria. IDH2 overexpression increased mitochondrial NADPH levels in ECs from thoracic aorta of old mice as determined by iNap1 fluorescence (Supplementary Fig. 5f–h). However, IDH2 overexpression failed to decrease mRNA levels of SASP genes (IL-1 β , IL-6, CCL2 and MMP9) in ECs from old mice. (Supplementary Fig. 5i). These results indicate that increasing mitochondrial NADPH metabolism cannot alleviate EC senescence.

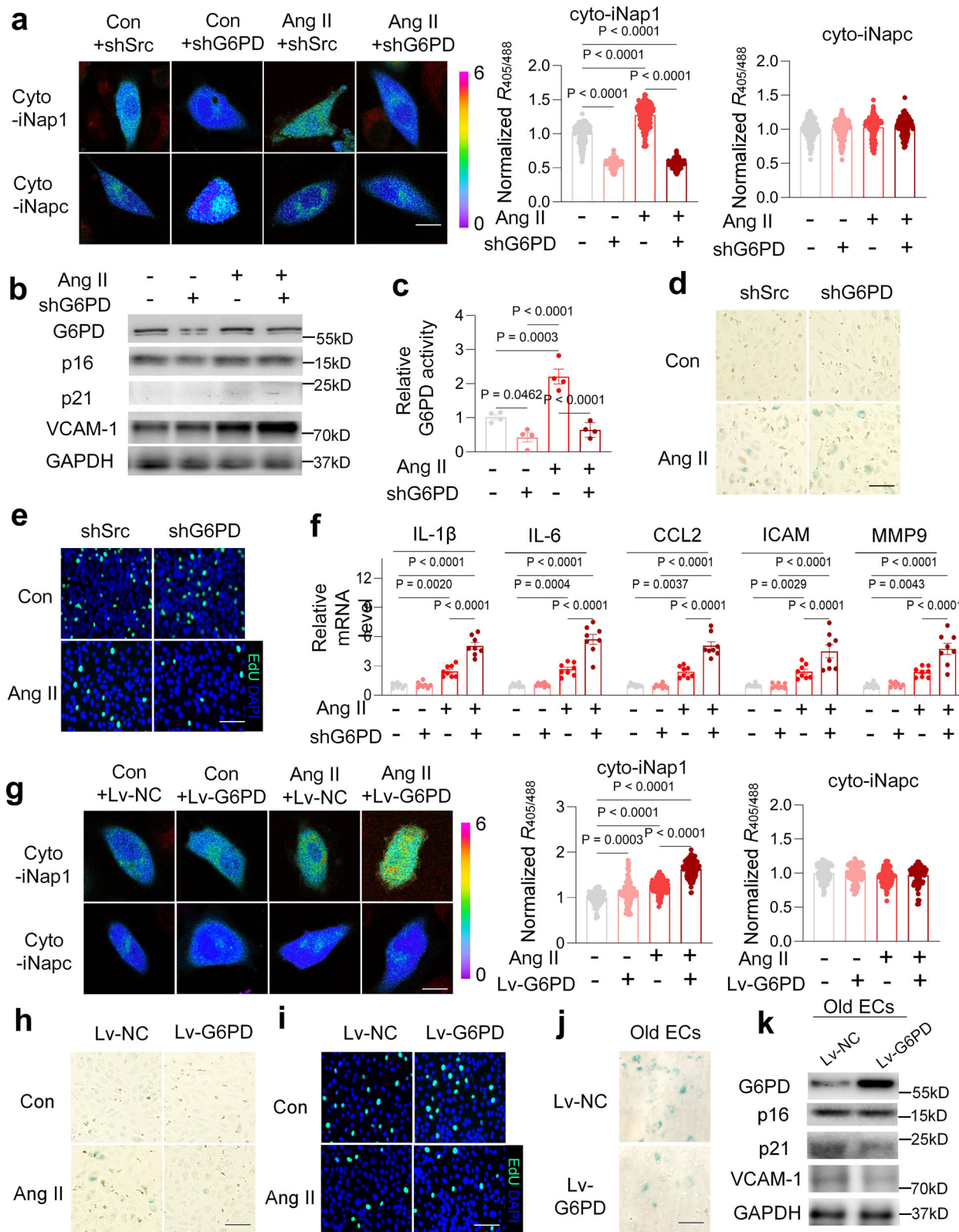
NADPH protected HAECS senescence through regulating glutathione redox and HDAC3 activity

To dissect the underlying mechanism by which NADPH ameliorates HAECS senescence, we first evaluated the role of ROS, which are widely considered to exacerbate cell senescence³⁸. A genetically encoded fluorescent sensor named roGFP1³⁹ was used to monitor glutathione redox potential (ratio of reduced and oxidized glutathione, GSH/GSSG) in HAECS. Ang II induced cytosolic oxidation as reflected by decreased roGFP1 ratio and G6PD overexpression reversed this effect (Fig. 4f). We also used an *in situ* fluorescent imaging method to analyze protein cysteinyl sulfhydryl redox state⁴⁰. Ang II increased global protein disulfide formation and G6PD overexpression blocked this effect (Supplementary Fig. 5j). Finally, TpNOX overexpression reversed the effects of G6PD on glutathione redox potential and protein cysteinyl sulfhydryl formation (Fig. 4f and Supplementary Fig. 5j). Therefore, NADPH may protect against Ang II-induced HAECS senescence via increasing GSH.

A recent study reported that NADPH directly bound HDAC3 and limited its activity on histone acetylation⁴¹. HDAC3 is an important regulator of central SASP genes (IL-1 β and IL-6)^{42,43}. Thus, we hypothesized that NADPH may prevent IL-1 β and IL-6 expression through binding HDAC3 in HAECS. To test this hypothesis, we monitored NADPH level in nucleus and performed drug affinity responsive target stability (DARTS) assay. We found that Ang II increased NADPH level in the nucleus (Supplementary Fig. 5k). NADPH bound and protected HDAC3 from degradation by pronase in a dose-dependent manner (Fig. 4g). Consistent with the results of DARTS assay, NADPH suppressed HDAC3 activity in a dose-dependent manner (Fig. 4h). Moreover, G6PD overexpression suppressed the increased HDAC3 activity by Ang II treatment, while TpNOX overexpression significantly elevated HDAC3 activity (Fig. 4i). In line with the changes of HDAC3 activity, the protein levels of acetylated H3 (Ac-H3) and acetylated H4 (Ac-H4) were increased in G6PD overexpressing and Ang II treated HAECS, and TpNOX overexpression blocked these effects (Fig. 4j and Supplementary Fig. 5l–n). Finally, G6PD overexpression blocked Ang II-induced nuclear factor kappa-B (NF- κ B) acetylation, which promotes SASP expression (Fig. 4j and Supplementary Fig. 5o). Indeed, G6PD overexpression suppressed Ang II-induced elevation of IL-1 β and IL-6 protein levels, and TpNOX overexpression reversed this blockade (Fig. 4j and Supplementary Fig. 5p, q). Taken together, NADPH alleviated Ang II-induced HAECS senescence through suppressing HDAC3 activity.

Upregulation of endothelial G6PD alleviated vascular aging

To determine whether upregulation of G6PD-mediated NADPH generation can prevent vascular aging, we constructed EC-specific adeno-associated virus with Tie promoter (AAV) containing G6PD (AAV-G6PD) or its negative control (AAV-NC). One week after tail vein injection of AAV-G6PD or AAV-NC (5×10^{11} GC/mouse), mice were infused with Ang II (1.5 mg/kg/day) for 4 weeks (Fig. 5a). Compared to AAV-NC mice, G6PD protein level and its activity were increased in



thoracic aorta of AAV-G6PD mice. In addition, G6PD protein level and its activity were further elevated in thoracic aorta of AAV-G6PD mice after Ang II infusion (Fig. 5b, c and Supplementary Fig. 6a). These results suggest that AAV-G6PD effectively infected mouse thoracic aorta. Compared to AAV-NC mice, G6PD overexpression significantly inhibited Ang II-induced increased vascular thickness, fibrosis and p21 immunofluorescence (Fig. 5d-f and Supplementary Fig. 6b-d). The

diastolic and systolic blood pressure of AAV-NC mice after Ang II infusion were higher than that in AAV-G6PD mice (Fig. 5g, h). Consistently, G6PD overexpression notably improved the impaired relaxation of thoracic aorta induced by Ang II (Fig. 5i). Moreover, the protein levels of aging markers (p16, VCAM-1 and p21) and mRNA levels of core SASP genes (IL-1 β , IL-6, IL-8 and CXCL1) were decreased in thoracic aorta of AAV-G6PD mice after Ang II infusion (Fig. 5j, k and

Fig. 3 | G6PD overexpression but not knockdown alleviated EC senescence.

a The fluorescence ratio of cyto-iNap1 and cyto-iNapc with or without Ang II and shG6PD overexpression in HAECS. $n = 3$ biologically independent samples, 167, 95, 123, 116, 158, 165, 151, and 147 cells for respective groups. Scale bar: 10 μ m. **b** G6PD, p16, p21 and VCAM-1 protein levels with or without Ang II and shG6PD overexpression in HAECS. **c** Relative G6PD activity with or without Ang II and shG6PD overexpression in HAECS. $n = 4$ biologically independent samples. **d** Representative SA- β -Gal staining images of HAECS with or without Ang II and shG6PD overexpression. Scale bar: 50 μ m. **e** Representative EdU fluorescence staining images of HAECS with or without Ang II and shG6PD overexpression. Scale bar: 50 μ m. **f** Relative mRNA levels of IL-1 β , IL-6, CCL2, ICAM and MMP9 with or without Ang II and shG6PD overexpression in HAECS. $n = 8$ biologically independent samples.

g The fluorescence ratio of cyto-iNap1 and cyto-iNapc with or without Ang II and G6PD overexpression in HAECS. $n = 3$ biologically independent samples, 103, 105, 111, 104, 124, 112, 114, and 101 cells for respective groups. Scale bar: 10 μ m. Representative SA- β -Gal (**h**) and EdU fluorescence (**i**) staining images of HAECS with or without Ang II and G6PD overexpression. Scale bar: 50 μ m. **j** Representative SA- β -Gal staining images of ECs isolated from thoracic aorta of old mice after G6PD overexpression. **k** G6PD, p16, p21 and VCAM-1 protein levels in ECs isolated from thoracic aorta of old mice after G6PD overexpression. Data are presented as mean values \pm SEM. Statistical significance was assessed by One-way ANOVA followed by Tukey's multiple comparisons test (**a, c, g**), Two-way ANOVA followed by Tukey's multiple comparisons test (**f**).

Supplementary Fig. 6e, f). To determine whether ROS mediated the protective effects of G6PD, we measured NADPH oxidase (Nox) activity, GSH and H₂O₂ levels in thoracic aorta. Interestingly, G6PD overexpression did not increase Nox activity, indicating that NADPH is not an activator of Nox. Ang II decreased GSH levels, increased the activity and protein levels of Nox as well as H₂O₂ levels. G6PD overexpression attenuated these effects (Fig. 5l-m and Supplementary Fig. 6g, h). These results suggest that G6PD upregulation in endothelium ameliorates vascular aging in vivo.

Folic acid elevated NADPH level via MTHFD1 to suppress EC senescence

Increasing NADPH level effectively alleviated vascular aging. However, NADPH is prone to oxidation and cannot be administered directly as a treatment. To quickly identify compounds that increase NADPH levels in cells, we developed a high-throughput screening system based on iNap1 fluorescence and screened 1419 FDA-approved drugs. First, iNap1 was expressed in primary cultured HAECS in 96-well black plates for 2 days. Then, the drugs were added and incubated for 0.5 hr and iNap1 fluorescence detected by using a high-content screening system (Fig. 6a). While majority of the screened drugs showed minimal impact on iNap1 fluorescence, we did identify 7 compounds (nicotinamide, aciclovir, dicumarol, thiamine hydrochloride, losartan potassium, olaparib, and folic acid) that significantly increased NADPH levels in HAECS. One of the compounds, folic acid (FA) possesses great potential for clinical use because it can be administered orally (Fig. 6b). We further found that FA (10 μ M) increased NADPH concentration in the cytosol of HAECS through one-carbon metabolism^{13,44} and iNapc fluorescence ratio remained unchanged (Fig. 6c). It has been reported that FA plays an important role in protecting against aging⁴⁵, but the effect of FA on vascular aging remains unknown. FA significantly suppressed Ang II-induced expression of aging biomarkers (p16, p21, and VCAM-1), reduced the increase of β -galactosidase, and promoted HAECS proliferation (Fig. 6e-f and Supplementary Fig. 7b-f). MTHFD1 is the only enzyme in FA metabolism pathway that generates NADPH in cytosol. We then knocked down MTHFD1 by using lentivirus containing shRNA (Lv-shM1), which did not alter the protein levels of p16, p21 and VCAM-1 in normal cultured HAECS (Fig. 6d and Supplementary Fig. 7a). FA failed to elevate cytosolic NADPH content in HAECS infected with Lv-shM1 (Fig. 6c). Moreover, Lv-shM1 attenuated the protective effects of FA on Ang II-induced HAECS senescence (Fig. 6e, f and Supplementary Fig. 7b-f). To further verify the anti-aging effect of FA, we isolated ECs from thoracic aorta of old mice (18 months old), infected them with Lv-shM1, and treated them with FA (10 μ M) for 2 days. We found that FA significantly prevented the increase of β -galactosidase (Fig. 6g and Supplementary Fig. 7g), facilitated cell proliferation (Fig. 6h and Supplementary Fig. 7h), and decreased protein levels of aging biomarkers (p16, p21, and VCAM-1, Fig. 6i and Supplementary Fig. 7i-k) and mRNA levels of SASP genes (IL-1 β , IL-6, IL-8 and CXCL1, Fig. 6j) in old ECs. Moreover, fluorescence indicators showed that FA elevated GSH level and diminished H₂O₂ in old ECs (Fig. 6k-l). These effects of FA in old ECs were abolished by Lv-shM1

overexpression. Similar effects on Nox activity were also obtained (Supplementary Fig. 7l). Taken together, FA elevates NADPH levels through MTHFD1 to effectively inhibit EC senescence (Supplementary Fig. 7m).

Folic acid increased NADPH level through MTHFD1 to alleviate Ang II-induced vascular aging

To further determine whether MTHFD1 mediates the anti-aging effects of FA in vivo, we constructed adeno-associated virus (AAV) containing MTHFD1 shRNA (AAV-shM1) driven by the EC-specific Tie promoter and a negative control construct (AAV-NC). One week after AAV-shM1 or AAV-NC (5×10^{11} GC/mouse) injection, FA (0.1 mg/kg/day) was administrated along with Ang II for 4 weeks (Fig. 7a). FA administration did not change the histology of kidneys and the brain (Supplementary Fig. 8a, b), as well as norepinephrine or catecholamine levels in the plasma (Supplementary Fig. 8c, d). AAV-shM1 decreased MTHFD1 protein level in homogenates of thoracic aorta (Fig. 7b and Supplementary Fig. 8e) but not in the media of thoracic aorta (Supplementary Fig. 8f). FA further elevated NADPH level in thoracic aorta in Ang II-treated group and AAV-shM1 prevented this increase, indicating that FA boosts NADPH generation through MTHFD1 in mouse thoracic aorta (Fig. 7c). FA prevented Ang II-induced increased vascular thickness, fibrosis and p21 immunofluorescence (Fig. 7d and Supplementary Fig. 8g-i). Ang II impaired endothelium-dependent vascular relaxation capacity and increased diastolic and systolic blood pressure. FA effectively rescued the impairment in blood pressure and relaxation ability (Fig. 7e, f). Furthermore, Ang II-induced increased protein levels of aging biomarkers (p16, p21 and VCAM-1, Fig. 7g and Supplementary Fig. 8j-l) and mRNA levels of SASP genes (IL-1 β , IL-6 and MMP3, Fig. 7h) were attenuated by FA. FA prevented Ang II-induced decreased GSH and increased H₂O₂ levels (Fig. 7i, j). The above anti-aging effects of FA were lost when MTHFD1 protein was knocked down by AAV-shM1 (Fig. 7c, j). FA also inhibited Ang II-induced increased Nox activity, which was restored by AAV-shM1 (Fig. 7k). Finally, FA did not elevate NAD⁺ content in mouse thoracic aorta, excluding NAD⁺ metabolism as a key mediator for FA's anti-aging effects (Fig. 7l). Taken together, FA increases NADPH content via MTHFD1 to alleviate Ang II-induced vascular aging in mice.

Folic acid ameliorated vascular aging in naturally aged mice

Ang II has broad functions in the body besides accelerating arterial aging and inducing age-related phenotypes in blood vessels. To further demonstrate the effects of FA on vascular aging in naturally aged mice, we orally administered FA (0.1 mg/kg/day) to mice at the age of 12 months for a year (Fig. 8a). FA elevated NADPH levels in thoracic aorta of old mice (Fig. 8b). Compared to young (4-month-old) mice, the vasculature of 24-month-old mice exhibited increased thickness, fibrosis, and increased p21 immunofluorescence, all of which were suppressed by 12-month FA feeding (Fig. 8c and Supplementary Fig. 9a-c). Although there were no significant changes in systolic and diastolic blood pressure in naturally aged mice, FA significantly improved vascular relaxation capacity in naturally aged mice

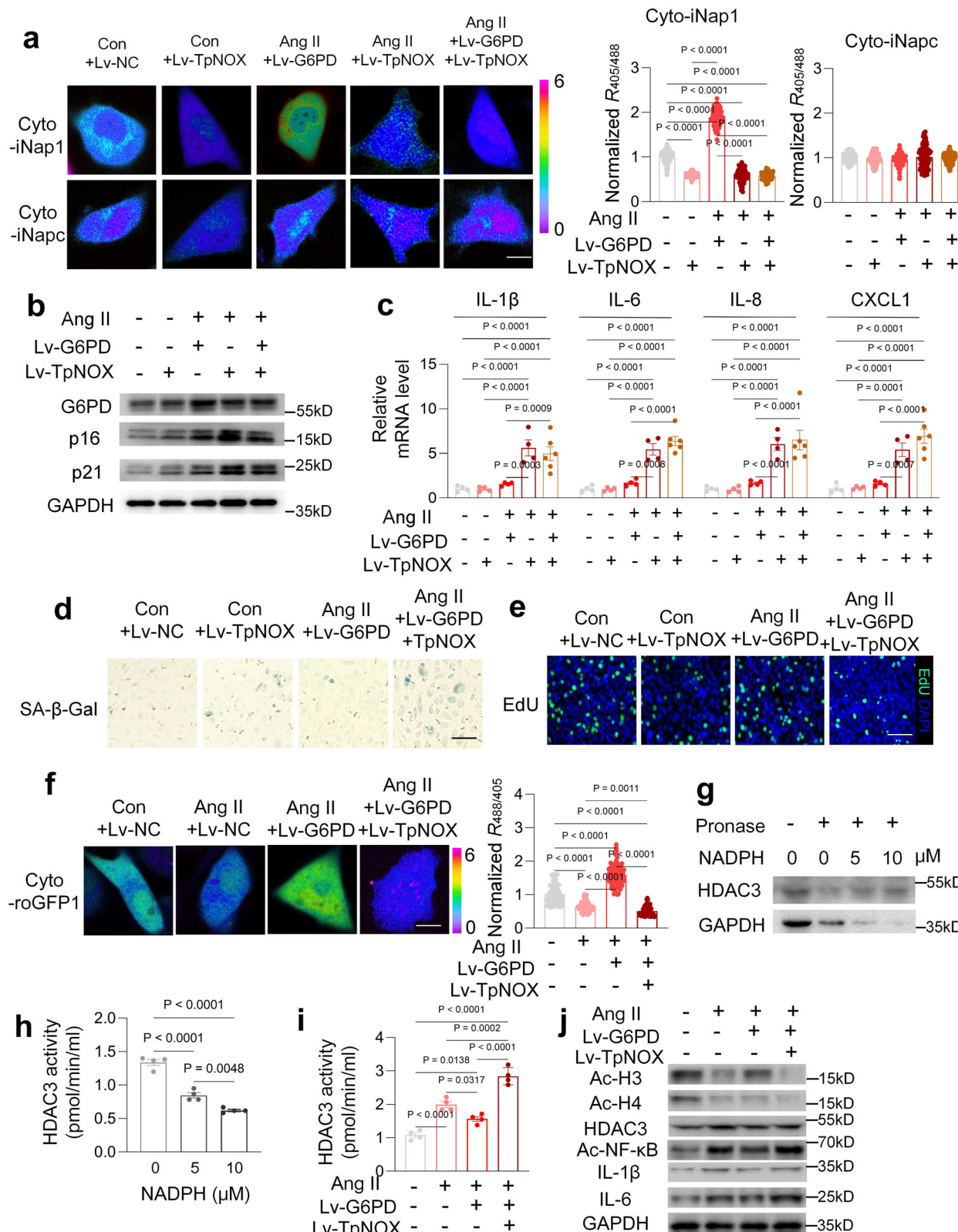


(Fig. 8d–f). FA also increased GSH level, decreased H_2O_2 level, and elevated Nox activity in naturally aged mice (Fig. 8g, h and Supplementary Fig. 9d). Moreover, the protein levels of aging biomarkers (p16, p21, and VCAM-1, Fig. 8i and Supplementary Fig. 9e–g) and mRNA levels of SASP genes (IL-1 β , IL-6, CCL2, ICAM1, MMP3, and MMP9, Fig. 8j) were lower in old mice with FA administration. In summary, FA alleviates vascular aging in naturally aged mice.

Discussion

In this study, we report an indispensable role of cytosolic NADPH in protecting against vascular endothelial aging. We used subcellular compartment-targeted indicators and detected increased cytosolic NADPH levels in primary cultured EC during senescence. Further, de-S-nitrosylation of G6PD at C385 is a site for regulating its protein stability, dimerization and NADPH generating activity. G6PD

Fig. 4 | NADPH was required for G6PD to protect against EC senescence. **a** The fluorescence ratio of cyto-iNap1 and cyto-iNapc with or without Ang II, TpNOX and G6PD overexpression in HAECS. $n = 3$ biologically independent samples, 116, 107, 112, 109, 119, 115, 111, 121, 106 and 155 cells for respective groups. Scale bar: 10 μ m. **b** G6PD, p16 and p21 protein levels in HAECS with or without Ang II, TpNOX and G6PD overexpression. **c** RT-PCR analysis of IL-1 β , IL-6, IL-8 and CXCL1 mRNA levels in HAECS with or without Ang II, TpNOX and G6PD overexpression. $n = 4$ biologically independent samples. Representative SA- β -Gal (**d**) and EdU fluorescence (**e**) staining images of HAECS with or without Ang II, TpNOX and G6PD overexpression. Scale bar: 50 μ m. **f** The fluorescence ratio of cyto-roGFP with or without Ang II, G6PD and TpNOX overexpression in HAECS. $n = 3$ biologically independent

samples, 100, 106, 104, and 90 cells for respective groups. Scale bar: 10 μ m. **g** HDAC3 protein levels in HAECS with or without pronase and increase amount of NADPH incubation. **h** HDAC3 activity in HAECS with increase amount of NADPH incubation. $n = 4$ biologically independent samples. **i** HDAC3 activity with or without Ang II, G6PD and TpNOX overexpression in HAECS. $n = 4$ biologically independent samples. **j** Ac-H3, Ac-H4, HDAC3, Ac-NF- κ B, IL-1 β and IL-6 protein levels with or without Ang II, G6PD and TpNOX overexpression in HAECS. Data are presented as mean values \pm SEM. Statistical significance was assessed by One-way ANOVA followed by Tukey's multiple comparisons test (**a, f, h, i**), Two-way ANOVA followed by Tukey's multiple comparisons test (**c**).

overexpression effectively elevated NADPH levels and prevented EC senescence in vitro and vascular aging in vivo. Ablation of NADPH reversed the protective effects of G6PD overexpression and exacerbated EC senescence. We also identified that FA boosts NADPH generation via MTHFD1. NADPH regulates GSH redox and directly binds HDAC3 to suppress central SASP genes (Fig. 8k). These results show that endothelial NADPH metabolism is a target for vascular aging.

While NAD(H) has been known to play an important role in vascular aging⁴⁶, whether NADP(H), an equally important cofactor, plays any roles in vascular aging remains elusive. Here we employed genetic biosensors and reported that increasing cytosolic, but not mitochondrial, NADPH plays a key role in alleviating EC senescence. Intracellular NADPH signaling is compartmentalized and distinctly regulated under pathophysiological conditions. Thus, methods such as enzymology, high-performance liquid chromatography, and radioisotope labeling are not suitable to investigate NADPH metabolism in live cells²¹. We used iNap1 and monitored dynamic changes in NADPH metabolism in primary cultured ECs. We found that cytosolic but not mitochondrial NADPH levels were significantly increased during EC senescence. Cytosolic NADPH is closely coupled to glucose metabolism. While it is known that metabolic reprogramming occurs during EC senescence, whether glucose metabolism is altered in senescent ECs remains controversial. Despite the abundance of oxygen in the vascular compartment⁷, ECs rely mainly on glycolysis for energy. It has been reported that glycolysis is unchanged during HUVEC senescence, despite increased glucose consumption and lactate production⁴⁷. Another study, however, showed senescence-associated decline in HUVEC glycolysis, which was reversed by overexpressing nuclear factor erythroid 2-related factor 2⁴⁸. Moreover, elevating aerobic glycolysis has been shown to limit ROS production in old HAECS⁴⁹. A reason for these controversial results may be associated with inappropriate methodology. To specifically determine whether glucose metabolism is altered during EC senescence, compartmentalized targeted NADH/NAD⁺ ratio indicator (SoNar) has been developed and widely used to monitor energy metabolism^{24,50,51}. Our results showed that glycolysis and oxidative phosphorylation were suppressed while NADPH metabolism boosted during HAECS senescence, supporting substantial metabolism reprogramming and a potential switch from glycolysis to oxPPP pathway. Our results suggest that NADPH is a more sensitive biomarker for senescence-associated phenotype and elevating NADPH generation could be a compensatory mechanism to slow down EC senescence through suppressing oxidative stress⁵².

This study also reveals an essential role of G6PD in protecting against vascular endothelial aging. G6PD is the primary source of cytosolic NADPH, which regulates cellular redox state and biological functions. For instance, G6PD overexpression increased NADPH and GSH levels, preventing aldosterone-induced ROS production in mouse aortic ECs⁵³. Elevating G6PD protein level also limited EC oxidative stress and potentiated NO concentration in primary vascular ECs⁵⁴. Oxidative stress is a fundamental cause of aging. Thus, targeting G6PD can benefit senescent EC through enhancing antioxidative defense. Indeed, transgenic mice overexpressing G6PD displayed extended lifespan in female²⁰ and alleviated age-related hearing loss¹⁹. G6PD

deficiency aggravated oxidant-induced cell senescence^{55,56}. Consistently, our results showed that G6PD overexpression ameliorated EC senescence and vascular aging through elevating GSH level and decreasing H₂O₂ level, while G6PD knockdown exacerbated EC senescence. It should be noted that excessive NADPH generation by G6PD may lead to redox stress and cellular dysfunction^{57,58}. Another group reported that blocking G6PD decreased NADPH levels and medial aortic thickness after 6-day Ang II fusion⁵⁹. This report used whole body G6PD-deficient mice and monitored Ang II's effect on aortic medial thickness, but not ROS, after 6 days of infusion. In our study, we manipulated G6PD specifically in vascular ECs and determined the effects on vascular function and ROS levels after Ang II infusion for 4 weeks. The different experimental conditions may cause the different findings. The delicate regulation of G6PD-mediated NADPH generation is critical to maintain vascular homeostasis.

G6PD phosphorylation⁶⁰, acetylation⁶¹ and O-GlcNAcylation⁶² have been reported previously. In this study we report that S-nitrosylation at C385 is a post-translational modification of G6PD. High levels of NO generated by eNOS orchestrate EC metabolism and function and decreased NO concentration triggers cell senescence^{5,63}. Since protein S-nitrosylation is sensitive to the intracellular redox state, decreased NO and de-S-nitrosylation of G6PD could be subsequent events during EC senescence. Interestingly, the C385 residues on the two G6PD monomers are close to each other and adjacent to NADP⁺ binding area, suggesting they may regulate G6PD activity. Indeed, our results showed that G6PD de-S-nitrosylation promoted its dimerization, potentiated its activity, stabilized the protein, and increased its protein level. The de-S-nitrosylation of G6PD could be a compensatory response to decreased NO and increased ROS generation during EC senescence. Future investigation is needed to determine the underlying mechanism by which de-S-nitrosylation stabilizes G6PD protein levels.

We also establish a causal link between G6PD and NADPH in protecting EC senescence. Besides generating NADPH, G6PD also regulates downstream signaling through binding other proteins. Since ablation of NADPH blocked the protective effect of G6PD overexpression, we concluded that G6PD overexpression alleviates vascular aging through NADPH. Increasing evidence shows that NADPH is not only critical for regulating glutathione redox system, but also governs many other signaling, including ferroptosis^{64,65} and disulfidoptosis⁶⁶. A recent report showed that NADPH directly bound HDAC3 to limit its activity⁴¹. HDAC3 regulates the de-acetylation of histone, and through which increases the expression of central SASP genes such as IL-1 β and IL-6^{43,67}. Our results suggested that NADPH suppressed HDAC3 activity to downregulate IL-1 β and IL-6 expression. Therefore, HDAC3 is a downstream mediator of NADPH in attenuating EC senescence.

We take advantage of the high sensitivity and strong fluorescence of iNap1 to conduct high-throughput screening in small-molecule libraries. Previously, high-throughput screening mainly relies on the activity of individual enzyme as a readout. The use of iNap1 monitored NADPH fluorescence as a readout has advantage because it converges multiple signaling pathways including PPP, folate metabolism and ME1

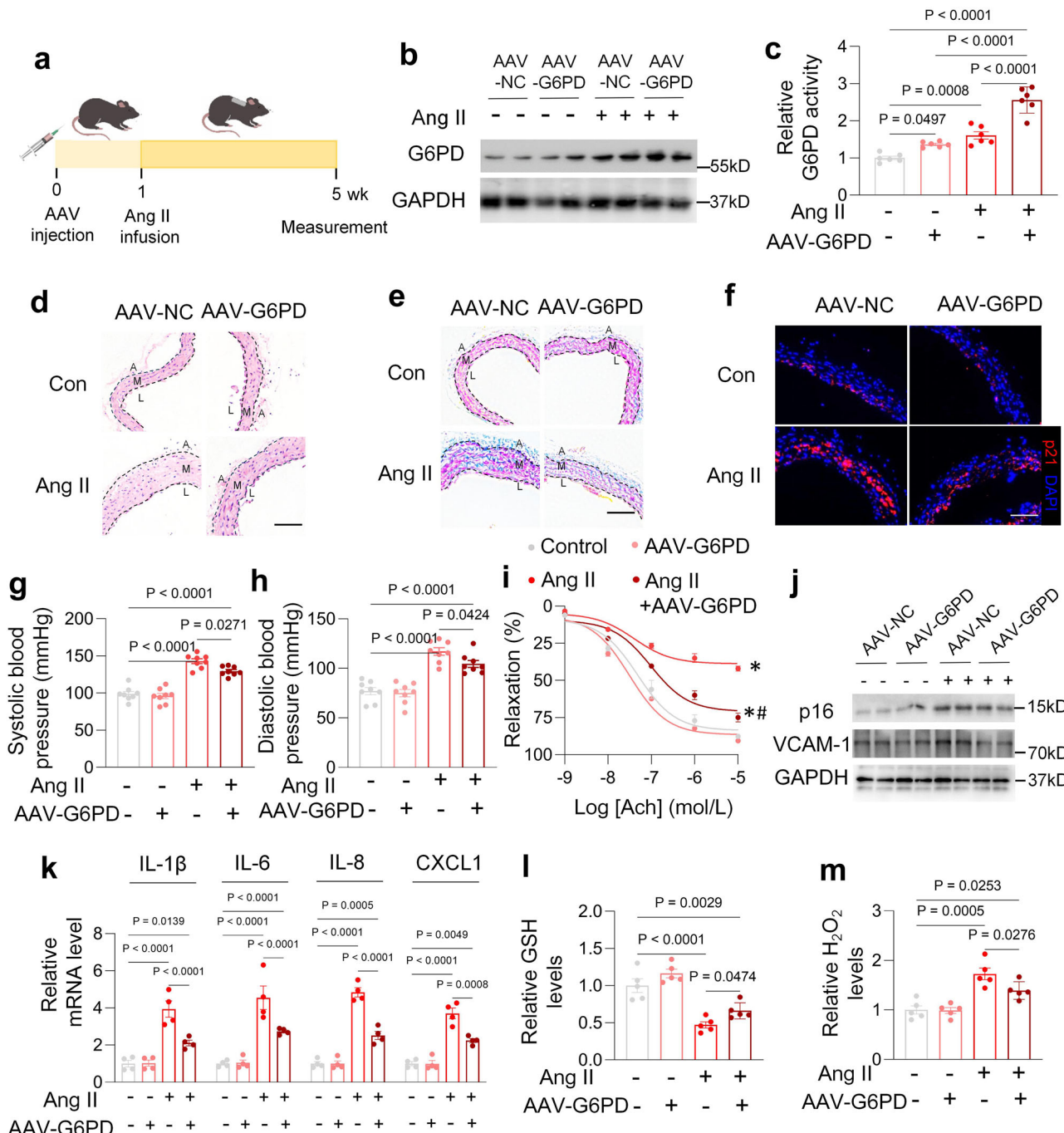


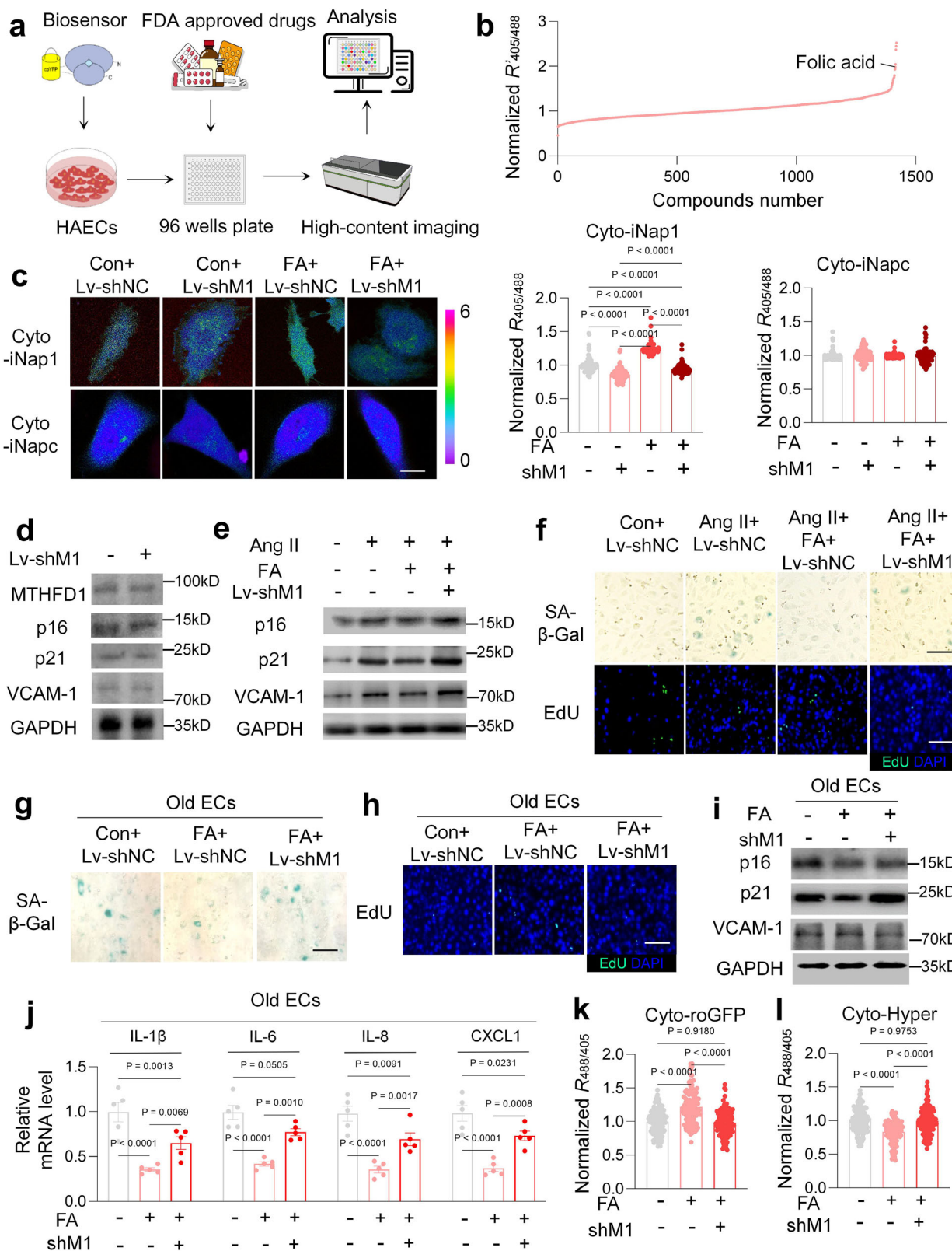
Fig. 5 | G6PD overexpression alleviated Ang II-induced vascular aging.

a Schematic demonstration of the experimental procedure. **b** G6PD protein levels in thoracic aorta with or without Ang II and G6PD overexpression. **c** Relative G6PD activity in mice with or without Ang II and G6PD overexpression. $n=6$ mice. Representative HE (**d**), Masson staining (**e**) and immunofluorescent staining of p21 (**f**) in thoracic aorta from mice with or without Ang II and G6PD overexpression. A: adventitia, M: media, and L: lumen. Scale bar: 100 μ m for (**d**, **e**), 50 μ m for (**f**). Systolic (**g**) and diastolic (**h**) pressure in mice with or without Ang II and G6PD overexpression. $n=8$ mice. **i** Relaxation activity of thoracic aorta from mice with or

without Ang II and G6PD overexpression. $n=5$ mice. * $p<0.0001$ vs control group. # $p<0.0001$ vs Ang II group. **j** p16 and VCAM-1 protein levels in thoracic aorta with or without Ang II and G6PD overexpression. **k** Relative mRNA levels of IL-1 β , IL-6, IL-8 and CXCL1 in thoracic aorta with or without Ang II and G6PD overexpression. $n=4$ mice. Relative GSH (**l**) and H₂O₂ (**m**) levels in thoracic aorta with or without Ang II and G6PD overexpression. $n=5$ mice. Data are presented as mean values \pm SEM. Statistical significance was assessed by Two-way ANOVA followed by Tukey's multiple comparisons test (**i**, **k**), One-way ANOVA followed by Tukey's multiple comparisons test (**c**) or Holm-Šídák's multiple comparisons test (**g**, **h**, **l**, **m**).

pathway^{11,13}. iNap1 also promptly responds to changes in intracellular NADPH level, which significantly shortens the time and cost of the screenings. The compound we identified through the screening, FA, is a common, FDA approved and widely used drug. Repurposing “old” drugs offers numerous benefits, such as saving a substantial amount of time and resources, and significantly accelerating drug development

process⁶⁸. We further showed that MTHFD1 is a key enzyme in folate metabolism pathway that catalyze FA to generate NADPH. Numerous reports have suggested that FA supports healthy life and lowers the risk of cardiovascular disease in the elderly⁶⁹. Our results link FA's beneficial effects to vascular aging. Because FA can be easily supplemented through food or as an oral drug, it has great potential to



become an efficient treatment for vascular aging. Future preclinical and clinical studies are warranted to establish its effectiveness in larger animals and in humans.

In summary, iNap1 sensor detected elevated cytosolic NADPH metabolism during EC senescence, which was mediated by G6PD de-S-nitrosylation. G6PD overexpression or FA supplementation abrogated vascular aging through augmenting NADPH metabolism. Based on

these findings, targeting endothelial NADPH metabolism may become a unique approach for vascular aging therapy.

Methods

Animals

C57BL/6 mice were purchased from Shanghai Jiesijie Laboratory Animal Co. Ltd and kept on regular chow and water ad libitum in a

Fig. 6 | Folic acid alleviated EC senescence via elevating NADPH metabolism.

a Schematic of iNap1 based high-throughput screening for compounds. **b** The effects of 1419 compounds on iNap1 fluorescence ratio over iNapc fluorescence ratio. **c** The fluorescence ratio of cyto-iNap1 and cyto-iNapc with or without FA and shM1 overexpression in HAECS. $n = 3$ biologically independent samples, 101, 110, 111, 131, 112, 108, 120, and 117 cells for respective groups. Scale bar: 10 μ m. **d** MTHFD1, p16, p21, and VCAM-1 protein levels in HAECS after shM1 overexpression. **e** p16, p21 and VCAM-1 protein levels with or without Ang II, FA and shM1 overexpression in HAECS. **f** Representative SA- β -Gal (upper) and EdU fluorescence (lower) staining images of HAECS with or without Ang II, FA and shM1 overexpression. Scale bar: 50 μ m. Representative SA- β -Gal (**g**) and EdU

fluorescence (**h**) staining images of old ECs with or without FA and shM1 overexpression. Scale bar: 50 μ m. **i** p16, p21 and VCAM-1 protein levels in old ECs with or without FA and shM1 overexpression. **j** RT-PCR analysis of IL-1 β , IL-6, IL-8 and CXCL1 mRNA levels in old ECs with or without FA and shM1 overexpression. $n = 5$ biologically independent samples. The fluorescence ratio of cyto-roGFP (**k**) and cyto-Hyper (**l**) with or without FA and shM1 overexpression in old ECs. $n = 3$ biologically independent samples, 122, 114, 117, 119, 117 and 118 cells for respective groups. Data are presented as mean values \pm SEM. Statistical significance was assessed by One-way ANOVA followed by Tukey's multiple comparisons test (**c, k, l**), Two-way ANOVA followed by Tukey's multiple comparisons test (**j**).

vivarium with 12 hr light/dark cycle at 22 °C. The mice were handled according to Guide for the Care and Use of Laboratory Animals published by the National Research Council Committee (United States). The animal experiment protocol was evaluated and approved by Animal Care and Use Committee of Shanghai University (ECSHU 2021-205).

For all animal experiments, both male and female mice were included in this study. The shG6 (mouse) (5'-GAGACTGCAATTCCGA-GATATCTGGAGATATCTCGGAATTGCACT CTCTTTTT-3'), shG6 (human) (5'-GCCTTCCATCAGTCGGATACTCGAGTATCCGACT GATG-GAAGGCTTTTT-3'), shM1 (mouse) (5'-GCTCTTTAATCGTCTGG-TACTCGAG TACCAGACGATTAAAGAGAGCTTTT-3') and shM1 (human) (5'-GCCATTGATGCTCG GATATTCTCGAGAAATATCCGAG CATCAATGGCTTTTT-3') were synthesized Genewiz Co. Ltd (Suzhou). The recombinant adeno-associated virus with EC-specific Tie promoter (AAV^{endo}) was generated by OBIO Technology Co. Ltd. (Shanghai). 8 weeks old mice were transduced with AAV^{endo}-negative control, AAV^{endo}-shM1, and AAV^{endo}-G6PD (5×10^{11} GC/mouse) through tail vein injection. After 1 week, the mice were infused with Ang II (1.5 mg/kg/day) or physiological saline (0.9% sodium chloride) infusion for 4 weeks. For Ang II-induced vascular aging, 0.1 mg/kg/day FA or 0.9% sodium chloride was administered by gavage for 4 weeks. For naturally aged mice experiments, bottles were prepared with water or FA solution (0.1 mg/kg/day) and the 12 months old mice fed water or FA for 12 months. The mice were euthanized with an intraperitoneal injection of a pentobarbital overdose (100 mg/kg).

Human

Human blood was collected from sex-, age- and body mass index (BMI)-matched participants at Shanghai Tongji Hospital. Plasma samples were stored in -80 °C, and NADPH or NAD⁺ contents were assessed via G6PD activity or alcohol dehydrogenase method (Beyotime Biotechnology, Cat. No. S0179 or Cat. No. S0175). The participants samples details were listed in Supplemental Table 1. All participants provided written informed consent to participate in the study and we obtained a written informed consent to publish potentially identifying information. The participants were voluntary and committed that they did not take vitamin B3 supplements or multivitamins for 14 days before this study. The human experiment protocol was evaluated and approved by Ethics Committee for Medical Research (Institutional Review Board) at Shanghai Tongji Hospital (K-2023-025).

Cells

Primary human aortic endothelial cells (HAECS) were purchased from ScienCell Research Laboratories. HAECS were grown in endothelial cell medium supplemented with basal medium, 5% fetal bovine serum, 1% cell growth factors (ScienCell Research, Cat. No.1001). HAECS at passages 3 to 7 were used in all experiments and the medium was refreshed every other day. Primary mouse aortic endothelial cells were isolated according to the method described previously⁷⁰. HEK293 and HEK293T cells were purchased from American type culture collection (ATCC, Cat. No. CRL1573 and CRL3216). All cells were maintained in a humidity-controlled environment (5% CO₂, 37 °C; Forma Scientific II).

Primary HAECS were passaged consecutively to induce replicative exhaustion. At 8th and 10th passages, the protein levels of senescence biomarkers (p16 and p21) were significantly increased (Supplementary Fig. 2f). We used 10th passage HAECS in this study.

Lentivirus virus production and infection

Lentivirus constructs (pLVX-cyto-iNap1, pLVX-mito-iNap3, pLVX-cyto-SoNar, pLVX-mito-SoNar, pLVX-cyto-Frex, pLVX-mito-Frex, pLVX-mito-IDH2, pLVX-cyto-roGFP, pLVX-cyto-Hyper, pLVX-G6PD, pLVX-G6PD C385A, pLVX-cyto-GefiNO, pLVX-cyto-iNapc, pLVX-mito-iNapc, pLVX-cyto-cpYFP, pLVX-mito-cpYFP, pLKO.1-G6PD shRNA and pLKO.1-MTHFD1 shRNA; 16 μ g) with helper vectors 12 μ g psPAX2 and 4 μ g pMD2.G were cotransfected into HEK293T cells with 7 μ l of HieffTM Trans liposomal transfection reagent (Yeasen, Cat. No. 40802). After 48 h and 72 h, lentiviral supernatants were collected and filtered. HAECS were subjected to infection with collected lentivirus with 8 μ g/ml polybrene and centrifuged at 1000 g for 1 h, followed by maintaining cells at 37 °C in an incubator with 95% humidity and 5% CO₂.

G6PD and its mutants plasmids

The cDNA of G6PD gene (a kind gift from Dr. Tianlong Zhang, Shanghai University) contains a 515 aa human G6PD variant (NCBI reference sequence: NP_001346945.1) minors the first 27 aa at the N-terminal. The primers for site directed mutagenesis of G6PD are in Supplemental Table 2.

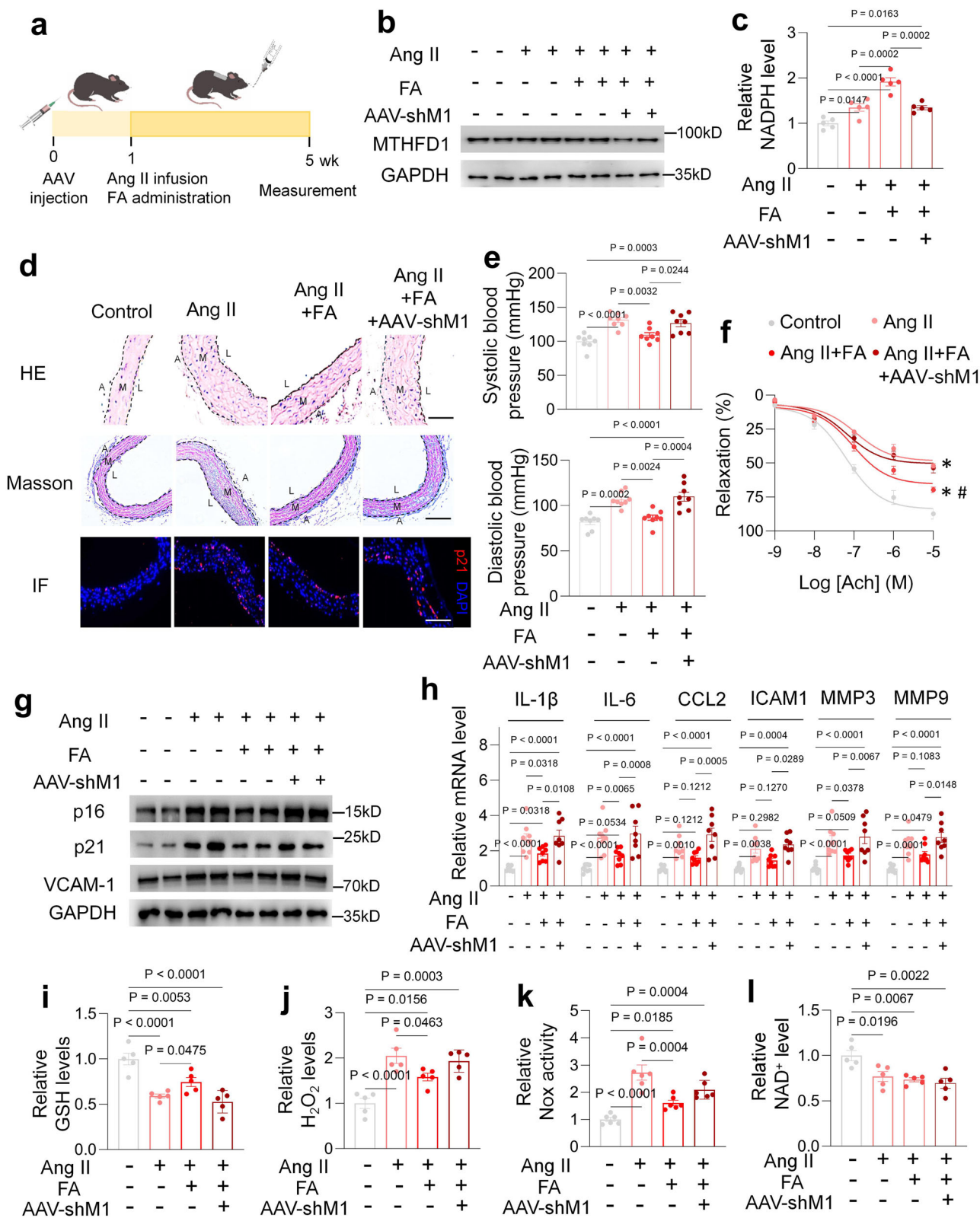
Confocal imaging

HAECS were plated on a 35 mm glass-bottom dish and the compartmental biosensors were expressed in ECs for 2 days. Images were acquired by a Leica SP8 confocal microscope with super-sensitive HyD detectors. Dual-excitation images of biosensors were taken by tandem excitation at 405 nm and 488 nm with an emission range of 500–560 nm. A 40 \times , 1.3 NA oil immersion objective was utilized. To monitor the dynamic changes of biosensors fluorescence ratio, 100 μ M diamide (Sigma-Aldrich, Cat. No. D3648) was directly added to the medium after the first image was taken. The pseudocolor images of biosensors fluorescence ratio were analyzed by ImageJ software.

In situ imaging of global thiol proteome redox state

The protein cysteinyl sulfhydryl redox state was measured according to a previous report⁴⁰.

To block protein thiols, methanol-fixed ECs were incubated with 200 mM iodoacetamide in 100 mM Tris (pH 8.3) and 5 mM EDTA at 37 °C for 1 h. The cells were washed six times with Tris buffer (pH 8.0) containing 5 mM EDTA. Then cells were incubated with 5 mM EDTA and 1 mM tris(2-carboxyethyl) phosphine (pH 8.3) at room temperature to reduce disulfides. One mM 5-iodoacetamido fluorescein in 100 mM Tris buffer was used to label the resulting thiols for 1 h. Excess dye was removed by washing the cells repeatedly with Tris buffer. DAPI was used to stain cell nuclei. Fluorescent images were taken with a Nikon fluorescence Ti2-E microscope. Fluorescence intensity was quantified by ImageJ, background fluorescence subtracted, and the



value normalized to cell number. Three fields were analyzed per experiment and 100 cells counted per sample.

Fluorescence measurements using microplate reader

Primary HAECS were seeded in a 96-well black plate for 12 h, and then biosensors lentiviruses infected the HAECS. After biosensors expression in HAECS for 2 days, the cells were washed twice and immersed in

HBSS buffer (pH = 7.4). The chemicals (100 μ M diamide, 10 μ M rotenone, 1 mM pyruvate, 5 mM oxamate, 1 mM β -hydroxybutyrate or 1 mM acetoacetic acid) were added as indicated in the Figures or figure legends. Dual-excitation fluorescence was obtained by an Infinite E Flex Microplate Reader (Tecan) with excitation at 420 nm and 485 nm, and emission at 520 nm. For *in situ* calibration of biosensors in primary HAECS, 0.001% or 0.3% digitonin was used to permeabilize cell

Fig. 7 | Folic acid abrogated Ang II-induced vascular aging via elevating NADPH metabolism. **a** Schematic demonstration of the experimental procedure. **b** MTHFD1 protein levels in thoracic aorta from mice with or without Ang II, FA and shM1 overexpression. **c** NADPH levels in thoracic aorta from mice with or without Ang II, FA and shM1 overexpression. $n = 5$ mice. **d** Representative images of HE (upper), Masson (middle) and p21 immunofluorescence (lower) in thoracic aorta from mice with or without Ang II, FA and shM1 overexpression. A: adventitia, M: media, L: lumen. **e** Systolic (upper) and diastolic (lower) pressure in mice with or without Ang II, FA and shM1 overexpression. $n = 8$ mice. Scale bar: 50 μ m for upper and lower, 100 μ m for middle. **f** Relaxation activity of thoracic aorta from mice with or without Ang II, FA and shM1 overexpression. $n = 5$ mice. $*p < 0.0001$ vs control

group, $^{\#}p < 0.0001$ vs Ang II group. **g** p16, p21 and VCAM-1 protein levels in thoracic aorta from mice with or without Ang II, FA and shM1 overexpression. **h** RT-PCR analysis of IL-1 β , IL-6, CCL2, ICAM1, MMP3 and MMP9 mRNA levels in thoracic aorta from mice with or without Ang II, FA and shM1 overexpression. $n = 8$ mice. GSH (**i**), H₂O₂ (**j**), Nox activity (**k**) and NAD $^{+}$ (**l**) levels in thoracic aorta from mice with or without Ang II, FA and shM1 overexpression. $n = 5$ mice for (**i, j, l**), 6 mice for (**k**). Data are presented as mean values \pm SEM. Statistical significance was assessed by Two-way ANOVA followed by Holm-Šídák's multiple comparisons test (**h**), One-way ANOVA followed by Tukey's multiple comparisons test (**c, e, l**), Holm-Šídák's multiple comparisons test (**i-k**).

membrane or mitochondrial membrane respectively. Different NADPH concentrations or NADH/NAD $^{+}$ ratios with same total NAD concentration (400 μ M) were directly added into permeabilized cells. After 15 min, the fluorescence was acquired by using a microplate fluorometer (excitation 420/485 nm and emission 520 nm).

High-content screening

Primary HAECS were seeded in a 96-well black glass bottom plate for 12 h and were infected by indicators lentiviruses for 2 days. 1419 FDA-approved drugs were purchased from TargetMol Chemicals Inc. and 100 μ M drugs were directly added into HAECS. After 0.5 h incubation at 37 °C with 5% CO₂, dual-excitation fluorescence was obtained by an Operetta CLS High Content Analysis System (PerkinElmer) with excitation at 405 nm and 488 nm, and emission range of 500–560 nm. Images were randomly taken, but HAECS with extraordinarily strong or low fluorescence levels were excluded for measurement.

SA- β -Gal staining

The β -galactosidase activity was analyzed by a Senescence β -galactosidase Staining Kit (Beyotime Biotechnology, Cat. No. C0602). Briefly, ECs were washed once with HBSS buffer and fixed with 4% paraformaldehyde for 15 min, and then cells were washed twice with HBSS. After washing, ECs were incubated with X-Gal solution at 37 °C for overnight. 5 random images were obtained by Nikon Eclipse Si microscope and SA- β -Gal positive cells were quantified by ImageJ.

Immunoblotting

ECs or vascular tissues were lysed in cell lysis buffer with a cocktail of proteinase/phosphatase inhibitors (Cell Signaling Technology, Cat. No. 5872). After centrifuge at 12,000 g for 20 min at 4 °C, equal amount of proteins were subjected to SDS-PAGE followed by transferring to 0.45 μ m PVDF membrane. The membrane was blocked with 5% non-fat milk in TBS buffer including 0.1% tween-20 for 1 hr at room temperature, and then sequentially incubated with primary antibodies at 4 °C overnight and HRP-conjugated secondary antibodies. Immunoblot images were acquired by Chemi-Image System (Tanon, 5200CE) with enhanced chemiluminescence substrate (Millipore, Cat. No. WBKLS0500). The intensity of bands was quantified by ImageJ and protein abundance was normalized to GAPDH protein level. We used the following primary antibodies: anti-p16 (1:2000, Proteintech, Cat. No. 10883-1-AP), anti-p21 (1:2000, Cell Signaling Technology, Cat. No. 37543), anti-VCAM-1 (1:2000, Proteintech, Cat. No. 11444-1-AP), anti-GAPDH (1:5000, Cell Signaling Technology, Cat. No. 2118S), anti-G6PD (1:2000, Cell Signaling Technology, Cat. No. 12263), anti-PGD (1:2000, Proteintech, Cat. No. 14718-1-AP), anti-IDH1 (1:2000, Proteintech, Cat. No. 12331-1-AP), anti-ME1 (1:2000, Proteintech, Cat. No. 16619-1-AP), anti-MTHFD1 (1:2000, Proteintech, Cat. No. 10794-1-AP), anti-Nox4 (1:2000, Proteintech, Cat. No. 14347-1-AP), anti-eNOS (1:2000, Cell Signaling Technology, Cat. No. 32027), anti-HDAC3 (1:2000, Cell Signaling Technology, Cat. No. 85057), anti- β -tubulin (1:3000, Proteintech, Cat. No. 10094-1-AP), anti-NADK (1:2000, Proteintech, Cat. No. 29290-1-AP), anti-acetyl-NF- κ B p65 (Lys310) (1:2000, Affinity, Cat. No. AF1017), anti-Ac-H3 (1:2000, Cell Signaling Technology, Cat. No.

8173), anti-Ac-H4 (1:2000, Cell Signaling Technology, Cat. No. 8647), anti-IL-1 β (1:2000, Cell Signaling Technology, Cat. No. 12242) and anti-IL-6 (1:2000, Proteintech, Cat. No. 21865-1-AP). The appropriate secondary antibodies: goat anti-mouse IgG antibody (1:10000, Invitrogen, Cat. No. 31430) and goat anti-rabbit IgG rabbit (1:10000, Invitrogen, Cat. No. 31460).

Biotin-switch analysis

The S-nitrosylation level of G6PD or total proteins was measured according to the manufacturer's instruction (Cayman Chemical, Cat. No. 10006518). Briefly, blocking buffer was added into cells and incubated for 30 min at 4 °C. After centrifugation for 10 min at 4 °C, the supernatants were mixed with 4 volumes of ice-cold acetone and incubated for 1 h at -20 °C. After centrifugation for 10 min at 4 °C, the supernatants were decanted, and the protein pellet was resuspended with 0.5 ml reducing and labeling reagents for 1 h incubation at room temperature. Biotinylated proteins were purified by incubation with avidin-coupled agarose beads at 4 °C for overnight. After centrifugation for 10 min at 4 °C, the supernatants were decanted, and the protein pellet was prepared for immunoblotting with G6PD antibody.

Real-time quantitative PCR

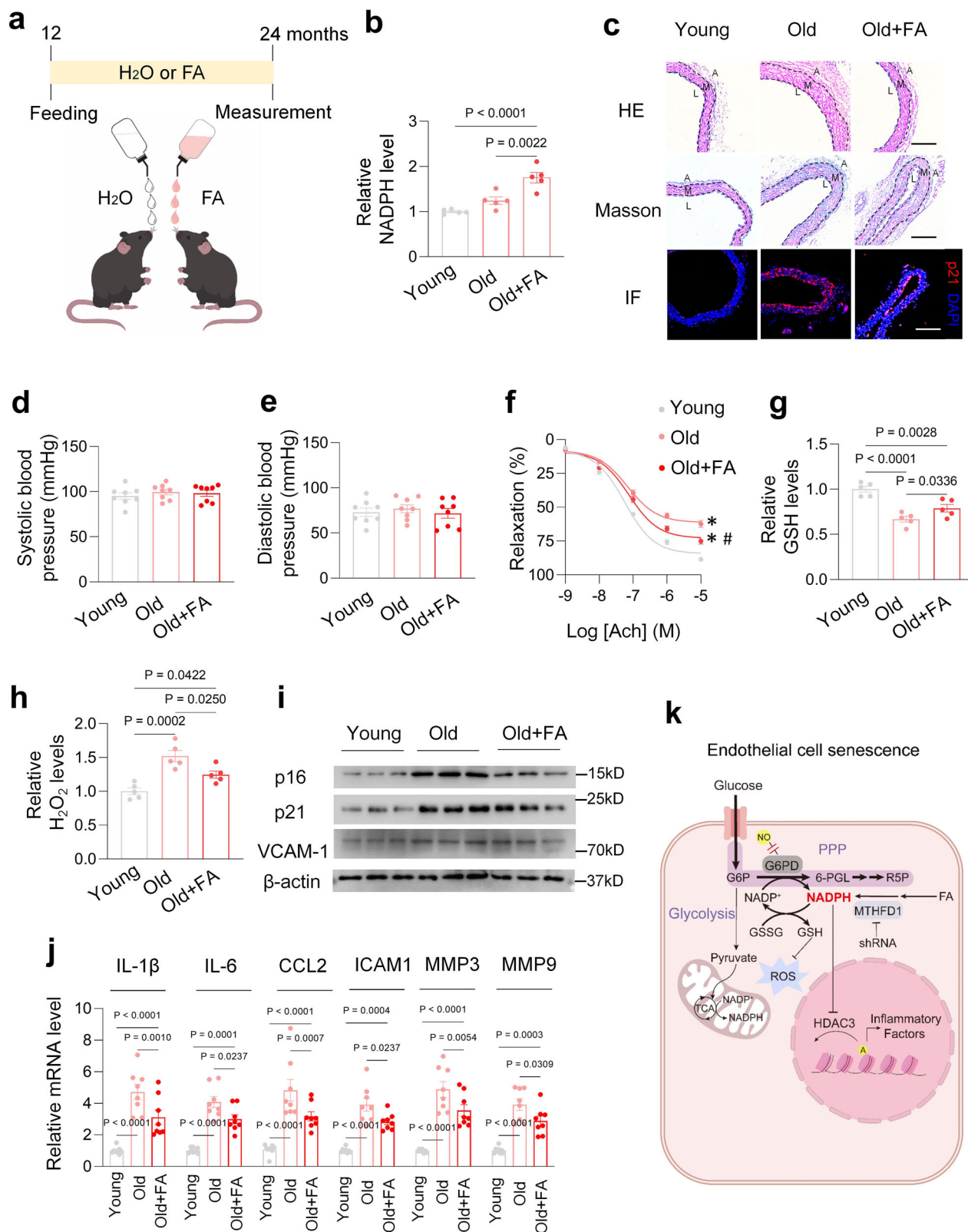
The total RNA was extracted from primary ECs or vascular tissues by a RNeasy extraction kit (Beyotime Biotechnology, Cat. No. R0026) according to the manufacturer's instruction. 1 μ g total RNA was reversed transcribed to cDNA using an Evo M-MLV RT Master Mix (Accurate Biology, Cat. No. AG11706) and quantified by the real-time PCR using SYBR Green Pro Taq HS Premix (Accurate Biology, Cat. No. AG11718) in ABI QuantStudio 3 Real-Time PCR System. The mRNA levels were normalized to the level of 18S RNA transcripts. The primer sequences used are in Supplemental Table 3.

NADPH and NAD $^{+}$ level analysis

NADPH levels were analyzed according to the manufacturer's instruction (Beyotime Biotechnology, Cat. No. S0179). Briefly, 1×10^6 ECs or 10 mg grinding tissue were dissolved with 200 μ l extraction buffer and centrifuged at 12,000 g with 4 °C for 10 min to remove cell debris and collected the supernatant. To exclude NADP $^{+}$ level, the supernatant was incubated at 60 °C for 30 min and then 50 μ l supernatant was mixed with 98 μ l NADP cycling buffer and 2 μ l NADP cycling enzyme for 5 min incubation at room temperature. 10 μ l NADPH developer was added and incubated at 37 °C for 20 min. The absorbance was determined using an Infinite E Plex Microplate Reader (Tecan) at 450 nm. NAD $^{+}$ levels were evaluated according to the manufacturer's instruction (Beyotime Biotechnology, Cat. No. S0175).

NADP $^{+}$ level analysis

ECs or the thoracic aorta were homogenized in a solution containing 80% methanol, 9% PBS and 11% H₂O. Aqueous extracts (10 mg) were collected after 13,000 g centrifugation at 4 °C for 10 min, and dried at 30 °C in a Speed-Vac. Liquid Chromatography (LC) separation was performed on Vanquish Core HPLC (UHPLC) and coupled to The TSQ Altis Plus mass spectrometer (Thermo Fisher Scientific) with an



electrospray ionization (ESI) source. LC separation was achieved on an Atlantis Premier BEH Z-HILIC (2.5 μ m, 2.1 \times 100 mm). 2 μ l of sample aliquot was injected into the column at 40 °C, the flow rate was set at 0.3 ml/min. Mobile phase A was 5 mM ammonium bicarbonate in H₂O, and Mobile phase B was 5 mM ammonium bicarbonate in ACN/ H₂O (90:10, v/v). The elution gradient started with 95 % phase B: 0–1 min 95 % B; 1–2.5 min 95%–75 % B; 2.5–4 min 75 % B; 4–4.5 min 75%–95 % B;

4.5–8 min 95 % B. The sample manager temperature was set at 4 °C. Experiments were conducted in negative ionization mode, and quantification was carried out in multiple reaction monitoring (MRM) mode. Mass spectrometric conditions including collision energy (CE) and RF lens voltage, were optimized automatically. The internal standard was 4-Chloro-Phenylalanine. The ion source conditions were listed as follows: Spray voltage, 3600 V; the ion transfer tube and the

Fig. 8 | Folic acid ameliorated vascular aging in naturally aged mice.

a Schematic of mice fed water or FA from 12 months old to 24 months old. **b** NADPH levels in thoracic aorta from old mice with or without FA. $n = 5$ mice. **c** Representative images of HE (upper), Masson (middle) and p21 immunofluorescence (lower) in thoracic aorta from 4-month-old mice and 24-month-old mice fed water or FA. A: adventitia, M: media, L: lumen. Scale bar: 100 μ m. Systolic (**d**) and diastolic (**e**) pressure in mice with or without FA. $n = 8$ mice. **f** Relaxation activity of thoracic aorta from 4-month-old mice and 24-month-old mice fed water or FA. $n = 5$ mice. * $p < 0.0001$ vs Young group, # $p < 0.0001$ vs Old group. GSH (**g**) and H₂O₂ (**h**) levels in thoracic aorta from 4-month-old mice and 24-month-old mice

fed water or FA. $n = 5$ mice. **i** Western blotting images showing p16, p21 and VCAM-1 protein levels in thoracic aorta from 4-month-old mice and 24-month-old mice fed water or FA. **j** RT-PCR analysis of IL-1 β , IL-6, CCL2, ICAM1, MMP3 and MMP9 mRNA levels in thoracic aorta from 4-month-old mice and 24-month-old mice fed water or FA. $n = 8$ mice. **k** Schematic model showing that G6PD de-S-nitrosylation or FA increased NADPH levels that regulated GSH redox and HDAC3 activity in EC senescence. Data are presented as mean values \pm SEM. Statistical significance was assessed by One-way ANOVA followed by Tukey's multiple comparisons test (**b, g, h**), Two-way ANOVA followed by Holm-Šidák's multiple comparisons test (**f, j**).

vaporizer temperature, 350 °C; sheath gas and auxiliary gas of nitrogen (purity \geq 99.99%) at the flow rate of 30 arb and 10 arb, respectively. Data were analyzed using the Xcalibur workstation (Version 4.5.445.18, Thermo Fisher Scientific).

GSH level analysis

GSH levels were analyzed by a reduced glutathione content assay kit according to the manufacturer's instruction (Solarbio, Cat. No. BC1175). Briefly, 10 mg grinding thoracic aorta were dissolved by 100 μ l extraction buffer and centrifuged at 8000 g, 4 °C for 10 min to remove cell debris and the supernatant was collected. Subsequently, 20 μ l supernatant was mixed with 140 μ l reaction buffer II and 40 μ l reaction III for 2 min incubation at room temperature. The absorbance was measured at 412 nm by using a microplate reader (Tecan, Infinite E Plex).

H₂O₂ level analysis

H₂O₂ levels were analyzed by a hydrogen peroxide content assay kit according to the manufacturer's instruction (Solarbio, Cat. No. BC3590). Briefly, 10 mg grinding thoracic aorta was dissolved by 100 μ l extraction buffer and centrifuged at 8000 g, 4 °C for 10 min to remove cell debris and the supernatant was collected. Subsequently, 80 μ l supernatant was mixed with 100 μ l reaction buffer II and 200 μ l reaction III and centrifuged at 4000 g, room temperature for 10 min. The supernatant was removed, and 1 ml reaction buffer IV was added into precipitation for 5 min incubation at room temperature. The absorbance was measured at 415 nm by using a microplate reader (Tecan, Infinite E Plex).

Nox activity analysis

Nox activity was analyzed by a commercial assay kit according to the manufacturer's instruction (Solarbio, Cat. No. BC0635). Briefly, 0.1 g grinding thoracic aorta were dissolved by 1 ml extract solution and 10 μ l Reagent III and centrifuged at 11,000 g for 10 minutes at 4 °C. Subsequently, 10 μ l supernatant was mixed with 175 μ l reagent IV, 25 μ l reagent IV and 40 μ l reagent VI. Reagent VI was replaced of distilled water at control group. The absorbance was measured at 600 nm by using a microplate reader at 37 °C (Tecan, Infinite E Plex) and recorded as A_{T1} for sample or A_{C1} for control. The plate was incubated at 37 °C water bath for 1 min and immediately measured the absorbance of final reaction which record as A_{T2} or A_{C2} , $\Delta A_T = A_{T1} - A_{T2}$, $\Delta A_C = A_{C1} - A_{C2}$. $\Delta A = \Delta A_T - \Delta A_C$. Nox Activity (U/mg prot) = $\Delta A \div 0.005 \times V_{\text{r}} \div C_{\text{p}} \times V_s \div T = 5000 \times \Delta A \div C_{\text{p}}$. V_{r} : Total reaction volume, 0.25 ml. C_{p} : Supernatant sample protein concentration (mg/ml). V_s : Sample volume (ml), 0.01 ml. T : Reaction time (min), 1 min.

G6PD activity assay

G6PD activity was measured according to the manufacturer's instruction (Beyotime Biotechnology, Cat. No. S0189). Briefly, 1×10^6 ECs or 10 mg grinding tissue were dissolved with 200 μ l extraction buffer and centrifuged at 12,000 g with 4 °C for 10 min to remove cell debris and collected the supernatant. 50 μ l supernatant was mixed with 50 μ l reaction buffer (1 mM MgCl₂, 50 mM Tris-HCl, 0.2 mM 6-phosphogluconate, 0.2 mM glucose-6-phosphate, 0.1 mM NADP⁺, 1.5 mM phenazine methosulfate, 0.5 mM MTT, pH = 8.0), and incubation at 37 °C for 30 min in the dark. The absorbance was determined using an Infinite E

Plex Microplate Reader (Tecan) at 450 nm. The G6PD activity was normalized to protein concentration.

NO and Nitrite contents measurement

A genetically encoded NO fluorescent sensor, GefiNO³⁰, was used to measure NO level in ECs. The cytosolic GefiNO were expressed in ECs for 2 days with or without Ang II. Images were acquired by a Nikon AX confocal microscope. Dual-excitation images of biosensors were taken by tandem excitation at 405 nm and 488 nm with an emission range of 500–560 nm. A 40x, 1.3 NA oil immersion objective was used. The pseudocolor images of biosensors' fluorescence ratio were analyzed by ImageJ software.

Nitrite content was analyzed according to the manufacturer's instruction (Beyotime Biotechnology, Cat. No. S0021). Briefly, 1×10^6 ECs were dissolved with 200 μ l extraction buffer and centrifuged at 12,000 g with 4 °C for 10 min to and remove cell debris and collect the supernatant. 50 μ l supernatant was sequentially mixed with 50 μ l griess reaction I and 50 μ l griess reaction II. The absorbance was determined using an Infinite E Plex Microplate Reader (Tecan) at 540 nm.

G6PD S-nitrosylation analysis

The peptide mixtures were analyzed by an Orbitrap Fusion Lumos Tribrid mass spectrometer (Thermo Fisher Scientific) coupled with an Easy-nLC 1000 nanoflow LC system (Thermo Fisher Scientific) as described previously with several modification⁷¹. In brief, a volume of 10 μ l sample was injected into instrument and separation was performed on a Thermo analytic column (Easy-Spray PepMap C18, 50 μ m \times 15 cm, 2 μ m). The mobile phase consisted of 0.1% formic acid (A) and 0.1% formic acid in acetonitrile (B). A gradient elution was used at a flow rate of 300 nL/min as follows: 0–5 min, 2% to 8% B; 5–90 min, 8% to 24% B; 90–110 min, 24% to 32% B; 110–115 min, 32%–90% B; 115–120 min, 90% B. The parameters for mass spectrometer were set as follows: MS spectra were acquired at a mass range of 350 m/z–1800 m/z in the orbitrap with 60,000 resolutions; automatic gain control (AGC) target was set as 1.0×10^6 ions with a maximum injection time of 50 ms. Data-dependent tandem MS analysis was performed using a cycle time of 3 s with multiple fragmentation methods. The collision energy for HCD was optimized at $30 \pm 5\%$. MS/MS spectra were acquired with a fixed first m/z of 100. The intensity threshold for fragmentation was set to 50,000 for orbitrap and included charge states from 2⁺ to 7⁺. The MS and MS/MS mass tolerances were set as 10 ppm and 0.02 Da, respectively. Protein identification was performed by searching tandem mass spectrometry against FastaDatabase (SwissProt_Human_201805.fasta) using SequestHT, which correlates experimental y- and b-ion fragment spectra with theoretical peptides sequences. In accordance with previous literature, cysteine residues modified by NO (+29 Da) or biotin-HPDP adducts (+428 Da) were characterized as S-nitrosylation modifications^{72,73}. Data were processed by Proteome Discoverer software (v. 2.1, Thermo Fisher Scientific).

Cell proliferation analysis

The cell proliferation was measured by a BeyoClick Edu-488 cell proliferation kit (Beyotime Biotechnology, Cat. No. C0071). Briefly, 10 μ M

5-Ethynyl-2'-deoxyuridine (EdU) was added into endothelial cell culture medium and incubated at humidity-controlled environment (37 °C, 5% CO₂). After 2 h incubation, the medium was removed, and cells were immersed in 4% paraformaldehyde for 15 min. Cells were washed three times with HBSS buffer and permeabilized with 0.2% Triton X-100 for 15 min. Cells were washed twice with HBSS buffer and click reaction buffer was added and incubated HAECs at room temperature in the dark for 30 min. After washing three times with HBSS buffer, nuclei were counterstained with DAPI. 5 random images were acquired by Nikon Eclipse Si microscope and EdU positive cells were quantified by ImageJ.

Histological assessment

Thoracic aorta were isolated from mice and immediately embedded in O.C.T. compounds (Tissue-Tek). 4% paraformaldehyde was used to fix 8 µm cryosections and then stained with Hematoxylin and Eosin (Yuanye Biotech, Cat No. R20570), or Masson's Trichrome (Yuanye Biotech, Cat No. R20379) according to the manufacturer's instruction. Images were obtained by Nikon Eclipse Si microscope and percentage of fibrosis was determined using ImageJ.

Immunofluorescence

Paraffin-embedded mouse thoracic aorta was dewaxed in xylene and rehydrated with gradient alcohols, and then thoracic aorta sections were immersed in 10 mM sodium citrate (pH 6.0) for antigen retrieval for 1 h. After washing three times with PBS buffer, tissue sections were blocked by blocking buffer (10% goat serum, 5% BSA and 0.5% Triton X-100 in PBS buffer) for 1 h at room temperature. Tissue sections were incubated with p21 antibody (1:200, Proteintech, Cat. No. 28248-1-AP) for overnight at 4 °C. After washing three times with PBS buffer, tissue sections were incubated Alexa Fluor 555-conjugated secondary antibody (1:500, Beyotime Biotechnology, Cat. No. A0453) for 1 h at room temperature in the dark. Nuclei were counterstained with DAPI. Images were acquired by Nikon Eclipse Si microscope and fluorescence of p21 protein were quantified by ImageJ.

Immunohistochemistry

Paraffin-embedded mouse thoracic aorta was dewaxed in xylene and rehydrated with gradient alcohols. Thoracic aorta sections were incubated with 3% H₂O₂ for 5 min and then washed by PBS for three times. The sections were immersed in 10 mM sodium citrate (pH 6.0) for antigen retrieval for 1 h. After washing two times with PBS buffer, tissue sections were blocked by blocking buffer (10% goat serum, 5% BSA and 0.5% Triton X-100 in PBS buffer) for 0.5 h at room temperature. Tissue sections were incubated with MTHFD1 antibody (1:200, Proteintech, Cat. No. 10794-1-AP) for overnight at 4 °C. After washing three times with PBS buffer, tissue sections were incubated with anti-rabbit antibody (1:500, Invitrogen, Cat. No. 31460) for 0.5 hr. The sections were washed by PBS for three times and then incubated with 3,3'-diaminobenzidine buffer for 10 min. After washing three times with PBS buffer, tissue sections were re-stained with hematoxylin for 5 min and immersed in 1% hydrochloric acid alcohol for seconds. Images were acquired by Nikon Eclipse Si microscope and MTHFD1 protein were quantified by Image-Pro Plus 6.0.

Aortic rings relaxation

Aortic aorta were freshly isolated from mice and immediately cleaned and cut into 3 mm length rings. The aortic rings were mounted in a chamber with physiological saline buffer (0.13 M NaCl, 4.69 mM KCl, 1.18 mM KH₂PO₄, 14.88 mM NaHCO₃, 5.55 mM glucose, 0.0263 mM EDTA, 1.6 mM CaCl₂) that linked myograph system (Danish Myo Technology A/S, Denmark). The rings were contracted by 1 µM phenylephrine and then dilated with cumulative levels of acetylcholine (10⁻⁹–10⁻⁵ M) to assess vascular reactivity.

Blood pressure

Blood pressure was determined by a CODA non-invasive blood pressure system (Kent Scientific Corp, US). Mice were trained and acclimated to the system, which including a heated platform (32 °C), a restrain tube and a cuff around the mouse tail. Placing the mouse in the holder and inflating the cuff lasted 5 min and then the mouse was placed back in its cage. Mice were trained 2–3 times prior to the measurement. The experiment was performed by the same person at the same time of the day. The parameters were set as: 20 cycles/set, 20 s of deflation time, and 5 acclimation cycles.

HDAC3 activity analysis

HDAC3 activity was determined according to the manufacturer's instruction (Biovision, Cat. No. K343). 25 µl substrate solution including short peptides with acetylated lysine residues was directly added to 25 µl samples and incubated for 30 min at 37 °C. 10 µl developer and 40 µl assay buffer were added into each well and incubated for 5 min at 37 °C. After incubation with developer solution, the fluorescence of samples and standards was measured by an Infinite E Plex Microplate Reader (Tecan) (Excitation 380 nm, Emission 500 nm), and the deacetylase activity was analyzed by standard curve.

Statistics

All data are expressed as Mean ± SEM. The animal numbers were indicated in the figure legend. GraphPad Prism 9.5.1 software for statistical analysis. Shapiro-Wilk normality test was performed for data distribution. Non-normally distributed data were assessed by Kruskal-Wallis test, followed by Mann-Whitney test for 2 groups or Dunn's post hoc analysis for >2 groups. Normally distributed data were analyzed by one-way analysis of variance (ANOVA), followed by Student's *t* test for 2 groups, Tukey's or Šidák's test for >2 groups. The data including two categorically independent variables and one dependent variable were two-way ANOVA. Multiple testing adjustment was included in Tukey's or Šidák's test and Dunn's test by controlling Type I error for the family of comparisons. A *P* value < 0.05 was considered statistically significant.

Reporting summary

Further information on research design is available in the Nature Portfolio Reporting Summary linked to this article.

Data availability

The data supporting the findings from this study are available within the manuscript and its supplementary information. Microarray data have been deposited at NCBI dataset under accession code BioProject: PRJNA1274883, <https://www.ncbi.nlm.nih.gov/bioproject/PRJNA1274883>. Source data are provided with this paper.

References

1. Vaduganathan, M., Mensah, G. A., Turco, J. V., Fuster, V. & Roth, G. A. The global burden of cardiovascular diseases and risk: a compass for future health. *J. Am. Coll. Cardiol.* **80**, 2361–2371 (2022).
2. Tsao, C. W. et al. Heart disease and stroke statistics-2022 update: a report from the american heart association. *Circulation* **145**, e153–e639 (2022).
3. Ding, Y. N., Wang, H. Y., Chen, H. Z. & Liu, D. P. Targeting senescent cells for vascular aging and related diseases. *J. Mol. Cell Cardiol.* **162**, 43–52 (2022).
4. Ungvari, Z. et al. Endothelial dysfunction and angiogenesis impairment in the ageing vasculature. *Nat. Rev. Cardiol.* **15**, 555–565 (2018).
5. Ungvari, Z., Tarantini, S., Donato, A. J., Galvan, V. & Csiszar, A. Mechanisms of vascular aging. *Circ. Res.* **123**, 849–867 (2018).
6. Pi, X., Xie, L. & Patterson, C. Emerging roles of vascular endothelium in metabolic homeostasis. *Circ. Res.* **123**, 477–494 (2018).

7. Falkenberg, K. D., Rohenova, K., Luo, Y. & Carmeliet, P. The metabolic engine of endothelial cells. *Nat. Metab.* **1**, 937–946 (2019).
8. Xiao, W. & Loscalzo, J. Metabolic responses to reductive stress. *Antioxid. Redox Signal.* **32**, 1330–1347 (2020).
9. Sies, H. & Jones, D. P. Reactive oxygen species (ROS) as pleiotropic physiological signalling agents. *Nat. Rev. Mol. Cell Biol.* **21**, 363–383 (2020).
10. Jia, G., Aroor, A. R., Jia, C. & Sowers, J. R. Endothelial cell senescence in aging-related vascular dysfunction. *Biochim. Biophys. Acta Mol. Basis Dis.* **1865**, 1802–1809 (2019).
11. Xiao, W., Wang, R. S., Handy, D. E. & Loscalzo, J. NAD(H) and NADP(H) redox couples and cellular energy metabolism. *Antioxid. Redox Signal.* **28**, 251–272 (2018).
12. Goodman, R. P., Calvo, S. E. & Mootha, V. K. Spatiotemporal compartmentalization of hepatic NADH and NADPH metabolism. *J. Biol. Chem.* **293**, 7508–7516 (2018).
13. Chen, L. et al. NADPH production by the oxidative pentose-phosphate pathway supports folate metabolism. *Nat. Metab.* **1**, 404–415 (2019).
14. Facchinello, N. et al. Oxidative pentose phosphate pathway controls vascular mural cell coverage by regulating extracellular matrix composition. *Nat. Metab.* **4**, 123–140 (2022).
15. Zhu, J. & Thompson, C. B. Metabolic regulation of cell growth and proliferation. *Nat. Rev. Mol. Cell Biol.* **20**, 436–450 (2019).
16. Xiao, W., Oldham, W. M., Priolo, C., Pandey, A. K. & Loscalzo, J. Immunometabolic endothelial phenotypes: integrating inflammation and glucose metabolism. *Circ. Res.* **129**, 9–29 (2021).
17. Li, X., Sun, X. & Carmeliet, P. Hallmarks of endothelial cell metabolism in health and disease. *Cell Metab.* **30**, 414–433 (2019).
18. Sabbatinielli, J. et al. Where metabolism meets senescence: focus on endothelial cells. *Front. Physiol.* **10**, 1523 (2019).
19. Bermudez-Munoz, J. M. et al. G6PD overexpression protects from oxidative stress and age-related hearing loss. *Aging Cell.* **19**, e13275 (2020).
20. Nobrega-Pereira, S. et al. G6PD protects from oxidative damage and improves healthspan in mice. *Nat. Commun.* **7**, 10894 (2016).
21. Choe, M. & Titov, D. V. Genetically encoded tools for measuring and manipulating metabolism. *Nat. Chem. Biol.* **18**, 451–460 (2022).
22. Tao, R. et al. Genetically encoded fluorescent sensors reveal dynamic regulation of NADPH metabolism. *Nat. Methods* **14**, 720–728 (2017).
23. Kane, A. E. & Sinclair, D. A. Sirtuins and NAD(+) in the development and treatment of metabolic and cardiovascular diseases. *Circ. Res.* **123**, 868–885 (2018).
24. Hu Q. et al. Genetically encoded biosensors for evaluating NAD(+)/NADH ratio in cytosolic and mitochondrial compartments. *Cell Rep. Methods* **1**, 100116 (2021).
25. Wang, M., Khazan, B. & Lakatta, E. G. Central arterial aging and angiotensin II signaling. *Curr. Hypertens. Rev.* **6**, 266–281 (2010).
26. Yang, D. et al. Histone methyltransferase Smyd3 is a new regulator for vascular senescence. *Aging Cell.* **19**, e13212 (2020).
27. Clement, J., Wong, M., Poljak, A., Sachdev, P. & Braidy, N. The plasma NAD(+) metabolome is dysregulated in “normal” aging. *Rejuvenation Res.* **22**, 121–130 (2019).
28. Zhao, Y. et al. Genetically encoded fluorescent sensors for intracellular NADH detection. *Cell Metab.* **14**, 555–566 (2011).
29. Farah, C., Michel, L. Y. M. & Baligand, J. L. Nitric oxide signalling in cardiovascular health and disease. *Nat. Rev. Cardiol.* **15**, 292–316 (2018).
30. Li, H. et al. A novel genetically encoded indicator for deciphering cytosolic and mitochondrial nitric oxide in live cells. *Biochem. Biophys. Res. Commun.* **749**, 151345 (2025).
31. Horikoshi N. et al. Long-range structural defects by pathogenic mutations in most severe glucose-6-phosphate dehydrogenase deficiency. *Proc Natl Acad Sci USA.* **118**, e2022790118(2021).
32. Wei, X., Kixmoeller, K., Baltrusaitis, E., Yang, X. & Marmorstein, R. Allosteric role of a structural NADP(+) molecule in glucose-6-phosphate dehydrogenase activity. *Proc. Natl. Acad. Sci. USA.* **119**, e2119695119 (2022).
33. Au, S. W., Gover, S., Lam, V. M. & Adams, M. J. Human glucose-6-phosphate dehydrogenase: the crystal structure reveals a structural NADP(+) molecule and provides insights into enzyme deficiency. *Structure* **8**, 293–303 (2000).
34. Jiang, P. et al. p53 regulates biosynthesis through direct inactivation of glucose-6-phosphate dehydrogenase. *Nat. Cell Biol.* **13**, 310–316 (2011).
35. Cosentino, C., Grieco, D. & Costanzo, V. ATM activates the pentose phosphate pathway promoting anti-oxidant defence and DNA repair. *EMBO J.* **30**, 546–555 (2011).
36. Zhong, B. et al. Glucose-6-phosphate dehydrogenase neutralizes stresses by supporting reductive glutamine metabolism and AMPK activation. *Signal. Transduct. Target Ther.* **6**, 46 (2021).
37. Cracan, V., Titov, D. V., Shen, H., Grabarek, Z. & Mootha, V. K. A genetically encoded tool for manipulation of NADP(+)/NADPH in living cells. *Nat. Chem. Biol.* **13**, 1088–1095 (2017).
38. Wiley, C. D. & Campisi, J. The metabolic roots of senescence: mechanisms and opportunities for intervention. *Nat. Metab.* **3**, 1290–1301 (2021).
39. Dooley, C. T. et al. Imaging dynamic redox changes in mammalian cells with green fluorescent protein indicators. *J. Biol. Chem.* **279**, 22284–22293 (2004).
40. Yang, Y., Song, Y. & Loscalzo, J. Regulation of the protein disulfide proteome by mitochondria in mammalian cells. *Proc. Natl. Acad. Sci. USA.* **104**, 10813–10817 (2007).
41. Li, W. et al. NADPH levels affect cellular epigenetic state by inhibiting HDAC3-Ncor complex. *Nat. Metab.* **3**, 75–89 (2021).
42. Ellmeier, W. & Seiser, C. Histone deacetylase function in CD4(+) T cells. *Nat. Rev. Immunol.* **18**, 617–634 (2018).
43. Chi, Z. et al. Histone deacetylase 3 couples mitochondria to drive IL-1beta-dependent inflammation by configuring fatty acid oxidation. *Mol. Cell.* **80**, 43–58.e7 (2020).
44. Fan, J. et al. Quantitative flux analysis reveals folate-dependent NADPH production. *Nature* **510**, 298–302 (2014).
45. Annibal, A. et al. Regulation of the one carbon folate cycle as a shared metabolic signature of longevity. *Nat. Commun.* **12**, 3486 (2021).
46. Covarrubias, A. J., Perrone, R., Grozio, A. & Verdin, E. NAD(+) metabolism and its roles in cellular processes during ageing. *Nat. Rev. Mol. Cell Biol.* **22**, 119–141 (2021).
47. Unterluggauer, H. et al. Premature senescence of human endothelial cells induced by inhibition of glutaminase. *Biogerontology* **9**, 247–259 (2008).
48. Kuosmanen, S. M., Sihvola, V., Kansanen, E., Kaikkonen, M. U. & Levonen, A. L. MicroRNAs mediate the senescence-associated decline of NRF2 in endothelial cells. *Redox Biol.* **18**, 77–83 (2018).
49. Borradaile, N. M. & Pickering, J. G. Nicotinamide phosphoribosyltransferase imparts human endothelial cells with extended replicative lifespan and enhanced angiogenic capacity in a high glucose environment. *Aging Cell.* **8**, 100–112 (2009).
50. Zhao, Y. et al. SoNar, a Highly Responsive NAD+/NADH Sensor, Allows High-Throughput Metabolic Screening of Anti-tumor Agents. *Cell Metab.* **21**, 777–789 (2015).
51. Wu, D., Tan, B., Sun, Y. & Hu, Q. Cystathionine gamma lyase S-sulphydrates Drp1 to ameliorate heart dysfunction. *Redox Biol.* **58**, 102519 (2022).
52. Kuehne, A. et al. Acute activation of oxidative pentose phosphate pathway as first-line response to oxidative stress in human skin cells. *Mol. Cell.* **59**, 359–371 (2015).
53. Leopold, J. A. et al. Aldosterone impairs vascular reactivity by decreasing glucose-6-phosphate dehydrogenase activity. *Nat. Med.* **13**, 189–197 (2007).

54. Leopold, J. A., Zhang, Y. Y., Scribner, A. W., Stanton, R. C. & Loscalzo, J. Glucose-6-phosphate dehydrogenase overexpression decreases endothelial cell oxidant stress and increases bioavailable nitric oxide. *Arterioscler. Thromb. Vasc. Biol.* **23**, 411–417 (2003).
55. Ho, H. Y. et al. Enhanced oxidative stress and accelerated cellular senescence in glucose-6-phosphate dehydrogenase (G6PD)-deficient human fibroblasts. *Free Radic. Biol. Med.* **29**, 156–169 (2000).
56. Cheng, M. L., Ho, H. Y., Wu, Y. H. & Chiu, D. T. Glucose-6-phosphate dehydrogenase-deficient cells show an increased propensity for oxidant-induced senescence. *Free Radic. Biol. Med.* **36**, 580–591 (2004).
57. Lee, J. W. et al. G6PD up-regulation promotes pancreatic beta-cell dysfunction. *Endocrinology* **152**, 793–803 (2011).
58. Tome, M. E., Johnson, D. B., Samulitis, B. K., Dorr, R. T. & Briehl, M. M. Glucose 6-phosphate dehydrogenase overexpression models glucose deprivation and sensitizes lymphoma cells to apoptosis. *Antioxid. Redox Signal.* **8**, 1315–1327 (2006).
59. Matsui, R. et al. Glucose-6 phosphate dehydrogenase deficiency decreases the vascular response to angiotensin II. *Circulation* **112**, 257–263 (2005).
60. Pan, S., World, C. J., Kovacs, C. J. & Berk, B. C. Glucose 6-phosphate dehydrogenase is regulated through c-Src-mediated tyrosine phosphorylation in endothelial cells. *Arterioscler Thromb. Vasc. Biol.* **29**, 895–901 (2009).
61. Wang, Y. P. et al. Regulation of G6PD acetylation by SIRT2 and KAT9 modulates NADPH homeostasis and cell survival during oxidative stress. *EMBO J.* **33**, 1304–1320 (2014).
62. Rao, X. et al. O-GlcNAcylation of G6PD promotes the pentose phosphate pathway and tumor growth. *Nat. Commun.* **6**, 8468 (2015).
63. Rizza, S. et al. S-nitrosylation drives cell senescence and aging in mammals by controlling mitochondrial dynamics and mitophagy. *Proc. Natl Acad. Sci. USA* **115**, E3388–E3397 (2018).
64. Nguyen, K. T. et al. The MARCHF6 E3 ubiquitin ligase acts as an NADPH sensor for the regulation of ferroptosis. *Nat. Cell Biol.* **24**, 1239–1251 (2022).
65. Ding, C. C. et al. MESH1 is a cytosolic NADPH phosphatase that regulates ferroptosis. *Nat. Metab.* **2**, 270–277 (2020).
66. Liu, X. et al. Actin cytoskeleton vulnerability to disulfide stress mediates disulfidoptosis. *Nat. Cell Biol.* **25**, 404–414 (2023).
67. Ho, M. et al. Targeting histone deacetylase 3 (HDAC3) in the bone marrow microenvironment inhibits multiple myeloma proliferation by modulating exosomes and IL-6 trans-signaling. *Leukemia* **34**, 196–209 (2020).
68. Pushpakom, S. et al. Drug repurposing: progress, challenges and recommendations. *Nat. Rev. Drug Discov.* **18**, 41–58 (2019).
69. Jenkins, D. J. A. et al. Supplemental vitamins and minerals for cardiovascular disease prevention and treatment: JACC focus seminar. *J. Am. Coll. Cardiol.* **77**, 423–436 (2021).
70. Wang J. M., Chen A. F. & Zhang K. Isolation and primary culture of mouse aortic endothelial cells. *J. Vis. Exp.* **118**, 52965 (2016).
71. Espadas G., Borras E., Chiva C. & Sabido E. Evaluation of different peptide fragmentation types and mass analyzers in data-dependent methods using an Orbitrap Fusion Lumos Tribrid mass spectrometer. *Proteomics* **17**, 1600416 (2017).
72. Greco, T. M. et al. Identification of S-nitrosylation motifs by site-specific mapping of the S-nitrosocysteine proteome in human vascular smooth muscle cells. *Proc. Natl. Acad. Sci. USA* **103**, 7420–7425 (2006).
73. Wang, Y., Liu, T., Wu, C. & Li, H. A strategy for direct identification of protein S-nitrosylation sites by quadrupole time-of-flight mass spectrometry. *J. Am. Soc. Mass Spectrom.* **19**, 1353–1360 (2008).

Acknowledgements

We thank Drs. Yi Yang and Yuzheng Zhao for providing the biosensors. We thank Drs. Deqiu Zhu and Tianlong Zhang for human sample collection and technical support respectively. This work was supported by the National Natural Science Foundation of China, China (82100405 to Q.H., 81703499 to D.W.), Science and Technology Commission of Shanghai Municipality, China (22ZR1456900 to D.W.), Shanghai Municipal Health Commission, China (2022YQ053 to D.W., 2021Y0268 to F.M.), Shanghai Pujiang Program, China (2020PJD055 to D.W.), Shuguang Hospital Research Funding Project, China (SG3915 to B.T.), Youth Innovation Promotion Association of Chinese Academy of Sciences (2020425 to T.C.), American Heart Association (18EIA33900041 to W.W.), Open Project of Qinghai Key Laboratory of Qinghai-Tibet Plateau Biology Resources (T.C. and Q.H.), Shanghai University School of Medicine Innovation Research Grant (Med-KC202509 to Q.H.).

Author contributions

Q.H. conceived the concept. Q.H., D.W. and W. W. designed the experiments. D.W., B.T., Z.C., Hq.L., Hm.L., and Y.Y. performed the experiments. Q.H., D.W., W.W., B.T., Y.Y., F.M., T.C. and X.D. analyzed the data. Q.H. and W.W. wrote the manuscript with inputs from all other authors.

Competing interests

The authors declare no competing interests.

Additional information

Supplementary information The online version contains supplementary material available at <https://doi.org/10.1038/s41467-025-64652-z>.

Correspondence and requests for materials should be addressed to Qingxun Hu.

Peer review information *Nature Communications* thanks Houzao Chen, Tomohiro Nakamura and the other, anonymous, reviewer for their contribution to the peer review of this work. A peer review file is available.

Reprints and permissions information is available at <http://www.nature.com/reprints>

Publisher's note Springer Nature remains neutral with regard to jurisdictional claims in published maps and institutional affiliations.

Open Access This article is licensed under a Creative Commons Attribution-NonCommercial-NoDerivatives 4.0 International License, which permits any non-commercial use, sharing, distribution and reproduction in any medium or format, as long as you give appropriate credit to the original author(s) and the source, provide a link to the Creative Commons licence, and indicate if you modified the licensed material. You do not have permission under this licence to share adapted material derived from this article or parts of it. The images or other third party material in this article are included in the article's Creative Commons licence, unless indicated otherwise in a credit line to the material. If material is not included in the article's Creative Commons licence and your intended use is not permitted by statutory regulation or exceeds the permitted use, you will need to obtain permission directly from the copyright holder. To view a copy of this licence, visit <http://creativecommons.org/licenses/by-nc-nd/4.0/>.

© The Author(s) 2025